Standard deviation in maximum restoring force controls the intrinsic strength of face-centered cubic multi-principal element alloys

Shuang, Fei; Laurenti, Luca; Dey, Poulumi

DOI
10.1016/j.actamat.2024.120508

Publication date
2025

Document Version
Final published version

Published in
Acta Materialia

Acta Materialia 282 (2025) 120508

Contents lists available at ScienceDirect

Acta Materialia

journal homepage: www.elsevier.com/locate/actamat

Standard deviation in maximum restoring force controls the intrinsic strength of face-centered cubic multi-principal element alloys

Fei Shuang [a,*], Luca Laurenti [b], Poulumi Dey [a,*]

[a] Department of Materials Science and Engineering, Faculty of Mechanical Engineering, Delft University of Technology, Mekelweg 2, 2628 CD Delft, the Netherlands
[b] Delft Centre of System and Control, Faculty of Mechanical Engineering, Delft University of Technology, Mekelweg 2, 2628 CD Delft, the Netherlands

ARTICLE INFO

Keywords:
Multi-principal element alloys
Maximum restoring force
Stochastic Peierls-Nabarro model
Symbolic machine learning
Rule-of-mixing

ABSTRACT

In this study, we explore the mechanisms underlying the exceptional intrinsic strength of face-centered cubic (FCC) Multi-Principal Element Alloys (MPEAs) using a multifaceted approach. Our methods integrate atomistic simulations, informed by both embedded-atom model and neural network potentials, with first-principles calculations, stochastic Peierls-Nabarro (PN) modeling, and symbolic machine learning. We identify a consistent, robust linear correlation between the strength of MPEAs and the standard deviation of the maximum stacking-fault restoring force ($\tau_{max,sd}$) across various potentials. This finding is substantiated by comparing the experimental strengths of Cantor alloys' subsystems and $Ni_{62.5}V_{37.5}$ against $\tau_{max,sd}$ values from high-throughput first-principle calculations. Our theoretical insights are derived from integrating the stochastic Peierls-Nabarro model with a shearable precipitation hardening framework, demonstrating that lattice distortion alone does not directly enhance intrinsic strength. Instead, $\tau_{max,sd}$ emerges as a critical determinant, capable of boosting the strength of MPEAs by up to tenfold. Our analysis reveals the critical role of the exponential form of the PN model in achieving substantial strength improvement by transforming the Gaussian-like distribution of τ_{max} into an exponential-like distribution of local Peierls stress. Additionally, using an advanced symbolic machine learning technique, the sure independence screening and sparsifying operator (SISSO) method, we derive interpretable relationships between MPEA strength, elastic properties, and τ_{max} statistics, offering new insights into the design and optimization of advanced MPEAs. These findings highlight that the nonlinear physics and atomic fluctuations characterizing MPEAs not only underpin their unconventional intrinsic strength but also contribute to other complex properties such as sluggish diffusion and cocktail effect.

1. Introduction

Multi-Principal Element Alloys (MPEAs), encompassing high-entropy alloys (HEAs) and medium-entropy alloys (MEAs), constitute an innovative class of materials renowned for their superior strength [1–4], ductility [5,6], fatigue resistance [7], corrosion resistance [8,9], hydrogen embrittlement resistance [10–12], and radiation resistance [13,14]. In particular, MPEAs exhibit remarkable potential for strengthening while retaining exceptional ductility and fracture toughness [15–17], even in extreme low-temperature environments [18]. One of the most intriguing deformation behaviors observed in MPEAs is characterized by wavy dislocation profiles and jerky motion within the slip planes [19,20]. Examining the mechanistic origin of these unique deformation mechanisms and their role in the exceptional strength of MPEAs are crucial for advancing our understanding of these intricate systems.

Most of existing strength models for MPEAs are based on the principles of solute solution strengthening (SSS), originating from the classical Labusch model [21]. This model predicts strength as $\sigma_c \sim f^{4/3}c^{2/3}$, where c represents the concentration of solute atoms and f signifies the interaction force between a solute atom and a dislocation. However, this model proves inadequate for MPEAs due to the challenge of distinguishing between solute and solvent atoms in MPEAs. Following attempts by Toda- Caraballo et al. [22], Varvenne et al. successfully extended the SSS theory to MPEAs by explicitly considering the interaction between solute and dislocation in an effective medium [23–25]. This theoretical framework has further been extended to consider twin strengthening in face-centered cubic (FCC) MPEAs [26], as well as edge and screw dislocation strengthening in body-centered cubic (BCC) MPEAs [27,28], along with solute strengthening of basal slip in Mg

* Corresponding authors.
E-mail addresses: F.Shuang@tudelft.nl (F. Shuang), P.dey@tudelft.nl (P. Dey).

https://doi.org/10.1016/j.actamat.2024.120508
Received 26 May 2024; Received in revised form 21 October 2024; Accepted 23 October 2024
Available online 2 November 2024

alloys [29]. More recently, the strengthening effect due to short-range order (SRO) has been incorporated based on this theory [30]. The pivotal parameter in this theory, solute-dislocation interaction energies, is typically derived using an average-atom (A-atom) interatomic potential [31,32], which is not easily accessible through experiments or first principle calculations based on density functional theory (DFT). Utilizing elasticity simplification, their models yield a Labusch-type expression for strength, i.e., $\sigma_c \sim \left[\sum_{\boldsymbol{r},n} f_n^2(\boldsymbol{r}) c_n\right]^{2/3}$, where n is the element index, and $\boldsymbol{r}$ is the position of a solute atom in the effective matrix relative to a dislocation. In these simplified theories, only elastic moduli, lattice constants, and solute misfit volumes are required [24]. While the Varvenne model has shown good agreement with experimental data for several MPEAs [24], recent findings have revealed a significant underestimation of the strength of equimolar CrCoNi when compared with simulations based on embedded-atom model (EAM) potential [33]. This discrepancy may arise from the absence of solute–solute interactions in the original Varvenne model as revealed by another recent simulation work [34]. Furthermore, Pei et al. proposed a theoretical model for accounting for the additional strengthening effect due to stacking fault energy fluctuation, which is simply linearly proportional to the standard deviation of stacking fault energy [35]. The resulting strength enhancement however is very small comparing existing simulation results (~40 MPa vs. ~400 MPa) [33,36], indicating that stacking fault energy fluctuation has minor effect on the strength enhancement of MPEAs.

Empirically, lattice distortion (LD) has conventionally served as a reliable indicator of the intrinsic strength of MPEAs [37–42]. Specifically, LD exhibits a linear relationship with the strength of MPEAs, represented as $\sigma_c \sim$ LD. Moreover, a recent study proposes a more accurate empirical relationship [37], $\sigma_c \approx \alpha\mu\gamma_{\mathrm{USF}} \times$ LD, where α is a constant coefficient, μ is the isotropic shear modulus, γ_{USF} is the average unstable stacking fault (USF) energy of the {110} plane of alloys. Remarkably, this model demonstrates reasonably accurate predictions for both yield strength and Vickers hardness across an experimental dataset comprising 83 yield strength and 28 hardness data points for BCC refractory MPEAs [37]. It is noteworthy that the rationale behind the LD-based prediction should align with the SSS model, as there are intrinsic connections between LD and misfit volume [43]. Additionally, LD has been observed to positively correlate with tensile fracture strain [44], but negatively correlate with compressive ductility in BCC refractory MPEAs [45]. One drawback of relying solely on LD is its failure to offer a comprehensive physical understanding that distinguishes MPEAs from traditional metals or alloys.

A novel approach developed to comprehend the behavior of MPEAs is the stochastic Peierls-Nabarro (SPN) model introduced by Zhang et al. [46]. Unlike the SSS model, the SPN model treats a long dislocation line in MPEAs as short segments with random properties. It then employs the classical PN model to examine each dislocation segment with random dislocation cores, which are disturbed due to complex atomic environments. Statistically, the intrinsic strength of MPEAs arises from the collective lattice friction of numerous short segments. Subsequent studies have provided rigorous mathematical proofs of the statistical distribution of elastic energy and misfit energy in the classical PN model [47], further considering the effect of SRO. While the existing SPN model lays down a foundational framework for deepening the understanding of the effects of randomness emerging from the atomic scale on the strength of MPEAs, it does not consistently align with the results of atomistic simulations [48,49]. This discrepancy may be attributed to the utilization of an oversimplified PN equation with dislocation width as the primary input. Consequently, the existing SPN method is not practical for predicting strength across the vast compositional space of MPEAs using readily calculable properties.

Alternatively, machine learning (ML) has recently been emerged as a powerful tool for investigating MPEAs by analyzing both experimental and computational data [50–52]. For example, various ML techniques such as Random Forest (RF) and Artificial Neural Networks (ANN) have been employed to predict the solid solution forming ability [53,54]. Furthermore, more comprehensive ML techniques including RF, ANN, Kernel Ridge Regression, Gaussian Process, and Support Vector Regression have been utilized to predict the hardness [55] and solid solution strengthening [56,57]. To address the black-box nature of conventional ML frameworks, symbolic machine learning, especially the Sure Independence Screening and Sparsifying Operator (SISSO) method, has been adopted to develop interpretable ML models for predicting properties such as elastic constants [58], stacking fault energies [59], and phase formation in MPEAs [60]. The successful application of SISSO in developing analytical models for these properties inspires confidence that similar approaches could predict the intrinsic strength of MPEAs based on the easy-to-compute inputs obtained by DFT calculations.

In this study, we propose utilizing the standard deviation of the maximum restoring force, $\tau_{\mathrm{max,sd}}$, as a robust indictor of MPEAs' strength. Our study confirms the general validity of the linear relationship between $\tau_{\mathrm{max,sd}}$ and MPEAs' strength across various atomistic simulations employing rule-of-mixing (ROM)-based EAM, DFT-fitted EAM, and neural network potential (NNP), as well as through comparisons with high-throughput DFT calculations and experimental data. Furthermore, we enhance the SPN model by incorporating a τ_{max}-dependent PN equation and a shearable precipitate model. This modification elucidates the pronounced nonlinearity of the PN model and the highly fluctuated τ_{max} as the mechanistic origin of the exceptional strength observed in MPEAs. Finally, we utilize SISSO to derive interpretable strengthening models for MPEAs based on the modified SPN model and extensive Monte Carlo simulations across a broad range of parameters. We utilize the comparison between the SSS and SPN models, along with a discussion of ROM in MPEAs and beyond, as a concluding remark for the paper.

2. Methods

2.1. Intrinsic strength determination by molecular statics simulations

We employ the periodic array of dislocation (PAD) model [61] to determine the intrinsic strength of MPEAs by capturing the critical shear stress required to initiate the motion of an edge dislocation, as depicted in Fig. 1. The crystallographic directions are x-[110], y-[$\bar{1}$11] and z-[1$\bar{1}$2], corresponding to the directions of dislocation glide, slip plane and dislocation line, respectively. The model has dimensions of around 30 × 20 × 20 nm^3, containing around 1 million atoms. Periodic boundary conditions are adopted in x-z plane and free boundary conditions are adopted in the y-direction. An edge dislocation is introduced into the middle slip plane of the model using Atomsk [62]. Five bottom layer atoms are fixed, while the atoms in the top five layers are displaced along the positive x-dislocation direction to induce shear strain on the model. The shear strain is incrementally applied to the system to alter the energy landscape of the dislocation movement. After each loading increment, the system's energy is minimized by the conjugate gradient (CG) method and the fast inertial relaxation engine (FIRE) method [63–65], and the resulting stress-displacement curves are documented to determine the intrinsic strength of MPEAs. This model has been extensively employed in prior studies for similar purposes [66–68]. The Large-scale Atomic/Molecular Massively Parallel Simulator (LAMMPS) package is used for all simulations [69]. OVITO is utilized for visualizing atomic configurations and post-processing results, such as extracting dislocation structures [70,71].

2.2. Interatomic potentials

Selecting appropriate interatomic potentials is crucial for ensuring reliable atomistic simulations, particularly for intricate MPEA systems [72]. Most previous studies have utilized the EAM database tool in

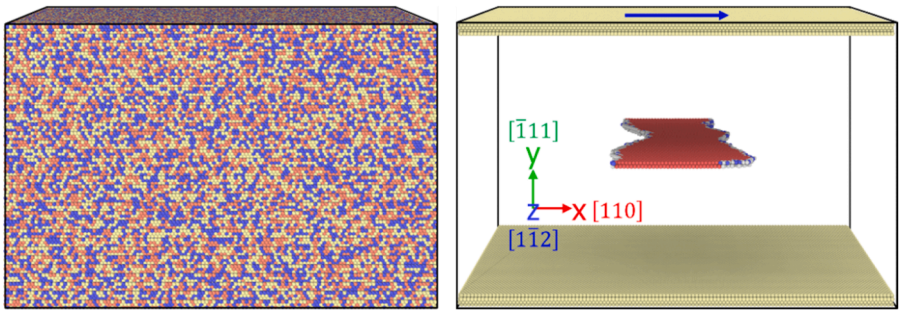

Fig. 1. The PAD model used to determine the intrinsic strength of FCC MPEAs under simple shear loading.

LAMMPS to generate toy EAM potentials based on pure metals, wherein the interactions between different elements are derived through ROM. Particularly, the EAM potential parameters developed by Zhou et al. [73,74] have been extensively employed to simulate various FCC and BCC MPEAs [27,28,75–79]. Two representative EAM potentials have been developed specifically for FCC quinary FeCoCrNiCu and FeCoCrNiAl MPEAs [80,81]. Additionally, several alloy potentials have been developed for MPEAs by fitting basic properties of pure metals and alloys obtained from DFT. These include EAM potentials for FeNiCr [82] and CrCoNi [33] systems, as well as modified embedded atom method (MEAM) potentials for FeMnCrCoNi systems [83]. Recently, machine learning has emerged as a powerful tool for describing interatomic interactions without relying on specific functional forms in MPEAs [84,85]. A notable example is the NNP developed to model the general deformation behavior of CrCoNi systems [86,87]. Although the training and prediction errors may be larger compared to other machine learning interatomic potentials (MLIPs) [88], this NNP stands as the sole existing potential capable of simulating the plastic deformation of CrCoNi. In this paper, we employ all three types of potentials—ROM-based EAM, DFT-fitted EAM, and NNP—to investigate the strengthening mechanisms of FCC MPEAs. The elements involved include Fe, Ni, Cr, Co, Cu, Al, Pd, and V. Table 1 provides a comprehensive list of the FCC MPEAs of interest and their corresponding potentials. These studies are particularly significant for elucidating the effects of interatomic potentials when exploring the deformation mechanisms of MPEAs, given that many previous works have relied on ROM-based EAM, which are considered as toy models and may not consistently align with DFT results.

2.3. First principle calculations

We utilize Vienna Ab initio Simulation Package (VASP) [89] to perform first principle calculations of unstable stacking fault energy (USFE) and maximum restoring force (τ_{max}) for 11 FCC MPEAs, including CoNi, FeNi, $Ni_{62.5}V_{37.5}$, FeCoNi, MnFeNi, MnCoNi, CrCoNi, VCoNi, MnFeCoNi, CrFeCoNi and CrMnCoNi. All systems are equimolar unless specified (e.g., $Ni_{62.5}V_{37.5}$). These alloys have been extensively studied in previous experiments, with intrinsic strength data readily available [41,90]. A gradient corrected functional in the Perdew-Burke-Ernzerhof (PBE) form is used to describe the exchange and correlation interactions [91]. Electron-ion interactions are treated within the projector-augmented-wave PAW method [92]. Standard PAW pseudopotentials distributed with VASP are adopted. The energy convergence is set to be 10^{-6} eV for electronic self-consistency calculations. All calculations are conducted without spin-polarization to facilitate high-throughput calculations.

Table 1
Interatomic potentials used for atomistic simulations of 16 FCC MPEAs.

	Systems	Potential files	Type
1	VNi-Zhou	VNi-Zhou.eam.alloy	ROM-EAM
2	VCoNi-Zhou	VCoNi-Zhou.alloy	ROM-EAM
3	FeCoNi-Zhou	FeCoNi-Zhou.alloy	ROM-EAM
4	FeCoNiCu-Zhou	FeCoNiCu-Zhou.alloy	ROM-EAM
5	FeCoNiCuAl-Zhou	FeCoNiCuAl-Zhou.alloy	ROM-EAM
6	FeCoNiCuPd-Zhou	FeCoNiCuPd-Zhou.alloy	ROM-EAM
7	FeCrCoNi-Farkas	FeNiCrCoAl-heaweight.setfl	ROM-EAM
8	FeCrNi-Farkas	FeNiCrCoAl-heaweight.setfl	ROM-EAM
9	FeCoNi-Farkas	FeNiCrCoAl-heaweight.setfl	ROM-EAM
10	FeNiCrCoAl-Farkas	FeNiCrCoAl-heaweight.setfl	ROM-EAM
11	FeNiCrCoCu-Farkas	FeNiCrCoCu-heafixed.setfl	ROM-EAM
12	FeCrNi-Bonny	FeNiCr.eam.alloy	DFT fitted
13	CrCoNi-Li	NiCoCr.lammps.eam	DFT fitted
14	CrCoNi-NNP	HDNNP	MLIP
15	CoNi-NNP	HDNNP	MLIP
16	CrCo-NNP	HDNNP	MLIP

Following the similar approach in Ref [93], a 72-atom supercell with 9 {111} layers are used for the calculations of USFE and τ_{max} as shown in Fig 2. Periodic boundary conditions are adopted for all three directions. A single stacking fault is introduced into the system by shearing the cell vector with a magnitude of [112]a/24 and [112]a/12 (a is the lattice constant), while keeping the atomic positions fixed. Three energies corresponding to configurations before shearing (E_0), after shearing [112]a/24 (E_1) and [112]a/12 (E_2) are computed. E_2 therefore represents the unstable stacking fault energy (USFE). τ_{max} is estimated by (E_1-E_0)/d, where d = [112]a/24. In order to obtain the reliable mean and standard deviation of τ_{max}, 50 random configurations are repeated for each system. It should be noted that lattice distortion is not considered here. Consequently, only single-point calculations are needed to obtain E_0. For E_1 and E_2, shearing the box decreases the distance between two adjacent two layers near the interface, such that it is necessary to release the stress along the z direction. To reduce the computational cost, we calculate five energies of E_1 and E_2 by gradually stretching the box (0, 0.167%, 0.333%, 0.500%, 0.667%) along the z direction for each configuration. E_1 and E_2 are obtained by finding the minimum value after spline interpolation of five energies. In total, we conduct 6050 single-point calculations to obtain reliable $USFE_{ave}$, $USFE_{sd}$, $\tau_{max,ave}$ and $\tau_{max,sd}$ for all 11 FCC MPEAs.

3. Correlation between atomic pining point strength and intrinsic strength in MPEAs

We first present the results of atomic pinning point strength, as depicted in Fig. 3. The simulation process remains consistent with previous work [19], with the inclusion of more general potentials discussed in Section 2.2. To be specific, all calculations are performed on a large, thin plate with dimensions of 25 × 25 × 5 nm^3 for different potentials, where the upper part is rigidly shifted to scan the {111} plane, as depicted in Fig. 3(a). The entire system is relaxed using CG, during which atoms exhibit no relative motion either within the upper or lower part. Fig. 3(b) showcases an example of the GSFE surface obtained for the configuration-averaged and for an individual atom in CrCoNi based on CrCoNi-Li. It is observed that, the overall GSFE surface appears smooth and uniform; however, at the atomic level, it exhibits significant fluctuation. The bottom panels of Fig. 3(b) depict the energy change

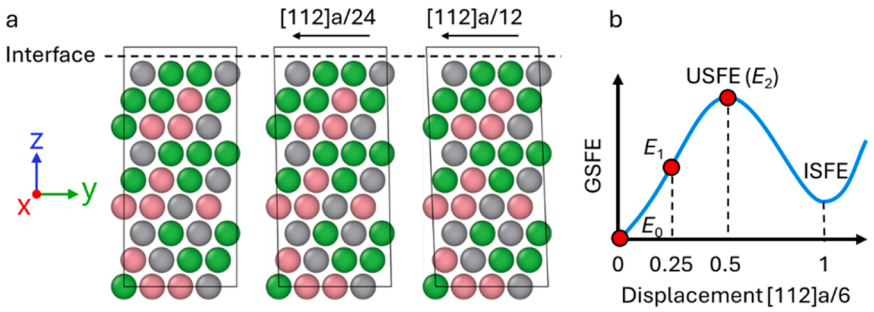

Fig. 2. (a) Simulation setup used to determine the maximum restoring force (τ_{max}) and USFE by DFT. (b) Schematic representation of GSFE curve.

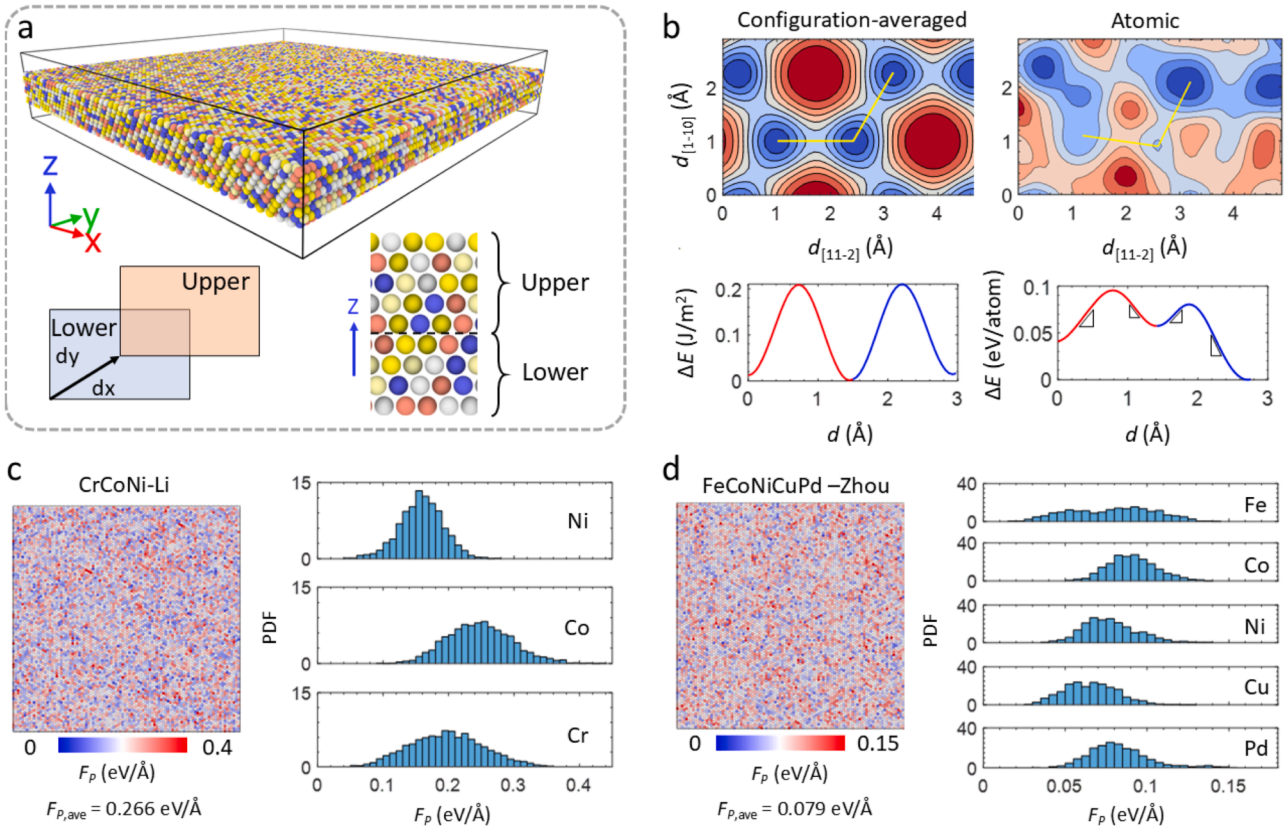

Fig. 3. (a) Schematic of atomic pining point strength calculation. (b) Configuration-averaged and atomic GSFE surface, as well as energy landscape along dislocation glide direction. Triangle symbols in the right bottom panel denote the maximum gradient of the curves. Random distribution of atomic pining strength in one {111} slip plane (left panel) and elemental distribution (right panel) in (c) CrCoNi-Li and (d) FeCoNiCuPd-Zhou.

along the dislocation glide path indicated by the yellow lines in the top panels. It is noteworthy that the energy landscape along these paths is highly distorted at the atomic scale. In accordance with the classical PN model [94], the critical factor influencing the lattice friction of metals is the maximum gradient of the GSFE curve, i.e., the maximum restoring force (τ_{max}). Following the convention in Ref [19], we refer to this atomic property as the atomic pining point strength (F_P) here. To visualize the distribution of F_P, we calculate the maximum F_P for four GSFE curve segments (right bottom panel in Fig. 3(b)) and map the corresponding values to each atom in CrCoNi-Li and FeCoNiCuPd-Zhou, as depicted in Fig. 3(c, d). Both of them exhibit a random distribution of F_P within the slip plane as seen in the left panels. The right panels display the statistical distribution of the F_P for each element. All distributions exhibit a resemblance to Gaussian distributions. Interestingly, as two common elements in these materials, Ni and Co display different F_P values in the right panels of Fig. 3(c, d), suggesting that F_P is a potential-dependent property.

We proceed to utilize the PAD model (Fig. 1) to determine the intrinsic strength of all MPEAs listed in Table 1. In Fig. 4(a), the stress-strain curves of two representative systems, CrCoNi-Li and FeCoNi-Zhou, are presented. The strength of MPEAs are defined as the maximum shear stress during deformation. CrCoNi-Li exhibits significantly higher strength than FeCoNi-Zhou. The dislocation structures at critical points are depicted in Fig. 4(b, c). CrCoNi-Li exhibits more jerky dislocation motion at high shear stresses, whereas FeCoNi-Zhou demonstrates relatively smooth dislocation motion at much lower stresses. Previous studies have unveiled a strong correlation between strength and the 95 percent of the atomic pinning point strength, denoted as $F_{P,95}$ [19]. We observe a similar trend in Fig. 4(d), but employing a broader range of potentials. Interestingly, we further identify an improved correlation between strength and the standard deviation of F_P ($F_{P,sd}$), as depicted in Fig. 4(e). Conversely, the plot of strength with respect to the average of F_P exhibits a weaker correlation. These results demonstrate that $F_{P,sd}$ serves as a more effective descriptor for representing the

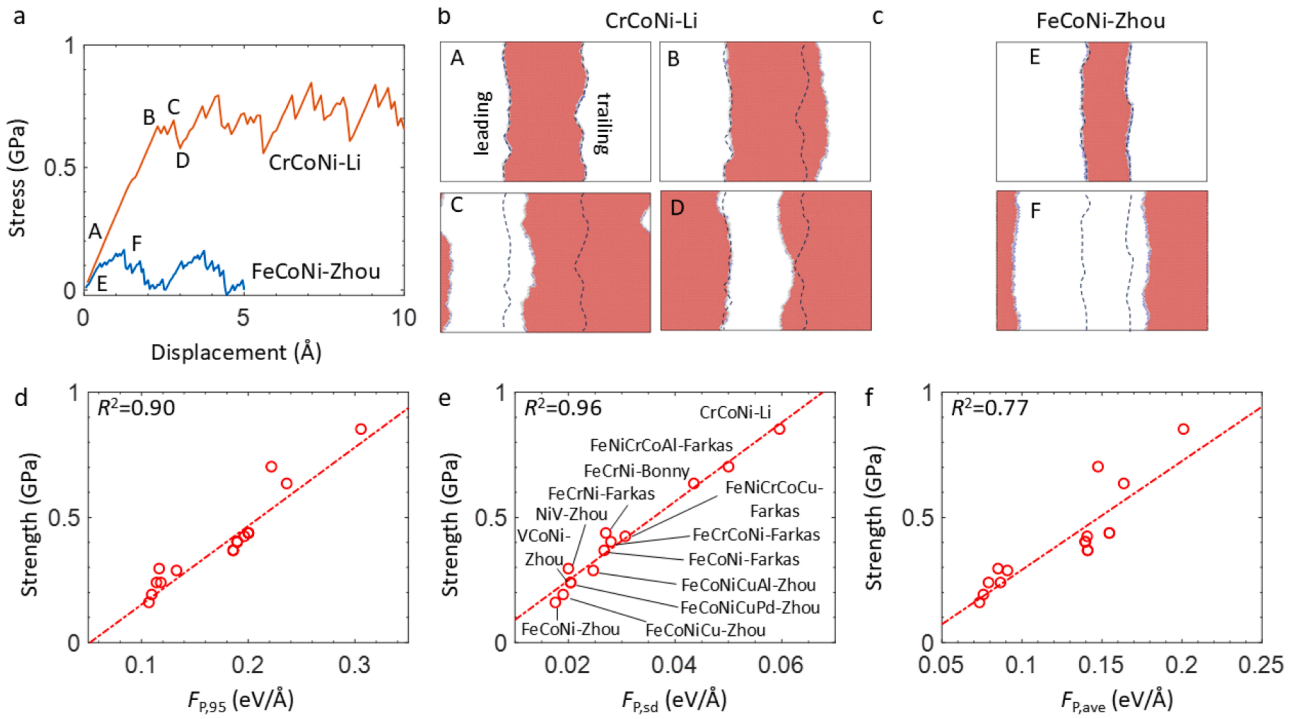

Fig. 4. (a) Shear stress vs. displacement curve for CrCoNi-Li and FeCoNi-Zhou. (b, c) Dislocation profiles at different deformation stages in these two systems. Correlations between strength with (d) 95th percentile, (e) standard deviation and (f) average of atomic pining point strength (F_P).

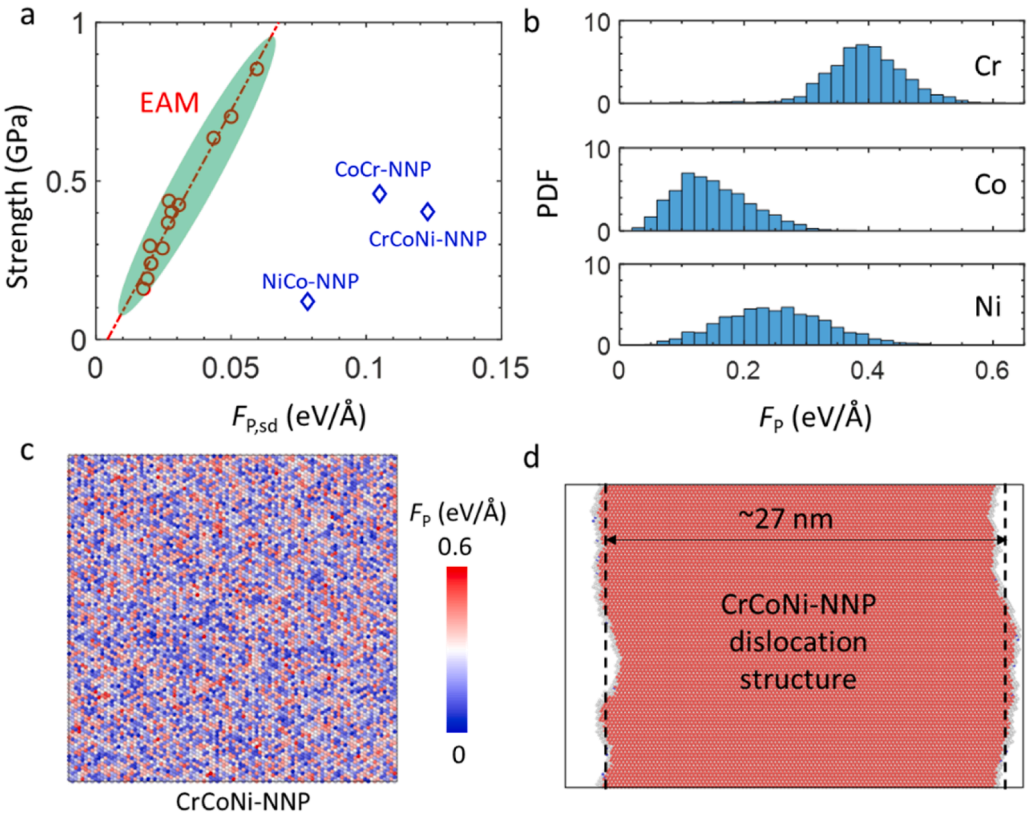

Fig. 5. (a) Correlation between strength and standard deviation of atomic pining point strength ($F_{P,sd}$) for all EAM-based simulations and NNP-based simulations. (b) Probability distribution of atomic pining point strength (F_P) for individual elements. (c) Random distribution of atomic pining strength in one {111} slip plane. (d) Edge dislocation profile in CrCoNi-NNP.

strength of MPEAs using different types of EAM potentials.

The atomic descriptor $F_{P,sd}$, however, is not applicable for CrCoNi systems using NNP. Fig. 5(a) illustrates that CrCo-NNP, CoNi-NNP, and CrCoNi-NNP do not conform to the trend observed with EAM potentials, suggesting that this relationship is not universal. Fig. 5(b) illustrates that the distributions of three elements, especially Cr, are markedly different from CrCoNi-Li in Fig. 3(c). Fig. 5(c) demonstrates that CrCoNi-NNP exhibits high atomic pinning point strength with a large standard deviation. The dislocation profile and the width of the stacking fault in Fig. 5(d) are also notably distinct from CrCoNi-Li in Fig. 4(b). Overall, these results highlight the distinctions between EAM potentials and NNP in modeling MPEAs.

4. Correlation between local-region pinning strength and intrinsic strength in MPEAs

To address the limitations of the atomic descriptor $F_{P,sd}$, we propose a new local-region pinning strength by calculating the maximum restoring force (τ_{max}) for a small supercell. This approach is particularly valuable for DFT calculations since DFT typically manages around 100 atoms. As an example, Fig. 6(a) illustrates one configuration with 240 atoms used for the calculation of CrCoNi-Li. Previous studies have employed this model to calculate GSFE curves for various FCC and BCC metals and MPEAs [93,95]. In the calculation of GSFE curve, the upper part is gradually displaced along the x-direction ($[\bar{1}12]$), followed by a constrained relaxation after each displacement. The calculation closely follows the procedure depicted in Fig. 3(a), but it is repeated for 10,000 random configurations. Observing the GSFE curves in Fig. 6(b), one can discern significant fluctuations around the average one (yellow curve). The statistical distribution of maximum restoring force (τ_{max}) is shown in Fig. 6(c). It is evident from the results that τ_{max} exhibits a Gaussian distribution but with left or negative skewness (−0.6), which indicates the presence of configurations with very low or nearly zero τ_{max}. It is interesting to note that the standard deviation in maximum restoring force ($\tau_{max,sd}$) for these small-scale configurations exhibits a strong correlation with the strength of MPEAs across all potentials, particularly including CrCoNi systems using NNP, as depicted in Fig. 6(d-f). Increasing the cross-sectional area of supercells (A) used for GSFE calculations results in a reduction of $\tau_{max,sd}$, yet the linear trend between strength and $\tau_{max\text{-}sd}$ persists. These results suggest that the local-region pinning strength, $\tau_{max\text{-}sd}$, serves as a more effective indictor to represent the strength of MPEAs.

To further validate the correlation between MPEAs' strength and $\tau_{max,sd}$, we repeat similar calculations for 155 stable FCC CrCoNi alloys based on EAM-Li. Fig. 7(a) illustrates that the strength is lower when MPEAs contain a higher proportion of Ni elements, while Fig. 7(b) indicates that the strength is primarily influenced by the concentration of Cr. Next, we explore the correlation between strength and various material properties. Fig. 7(c) shows that strength exhibits weak dependence on lattice distortion (LD). Furthermore, we find no correlation between strength and the standard deviation of intrinsic stacking fault energy (ISFE), as depicted in Fig. 7(d). This parameter has been proposed to account for the stacking fault strengthening of MPEAs in recent studies [35,48,96]. Finally, we unveil a strong linear correlation between strength and $USFE_{sd}$ and $\tau_{max\text{-}sd}$, as illustrated in Fig. 7(e, f). Note that strength ~ $USFE_{sd}$ is expected because τ_{max} is approximately proportional to USFE if GSFE curve has a sine function form (Fig. 2(b)). Overall, the universal existence of strength ~ $\tau_{max,sd}$ in the entire stable compositional space of CrCoNi systems in Fig. 7(f), as well as for MPEAs using different potentials in Fig. 6(d-f), demonstrates $\tau_{max,sd}$ as a reliable parameter for strength prediction in MPEAs.

One interesting observation is that the strengths of MPEAs exhibit a stronger correlation with EAM-based $F_{P,sd}$ in Fig. 4(e) than local-region pining strength $\tau_{max,sd}$ in Fig. 6(d-f) and Fig. 7(f). From the perspective of calculation process, $F_{P,sd}$ is the energy change of individual atoms, while $\tau_{max,sd}$ mirrors the energy variation of several atoms near the slip plane. Therefore, $F_{P,sd}$ has the higher resolution to capture the atomic details of strength of MPEAs than $\tau_{max,sd}$, resulting in the stronger correlation in Fig. 4(e). However, it is essential to note that this relationship holds true solely within the framework of the embedded atom model [97]. Fig. 5(a) illustrates that three subsystems of CrCoNi MPEAs employing NNP deviate from the trend of EAM. Specifically, CrCoNi-NNP exhibits a higher $F_{P,sd}$ compared to CrCo-NNP but displays a lower strength than CrCo-NNP. This suggests that $F_{P,sd}$ and $\tau_{max,sd}$ are not correlated factors

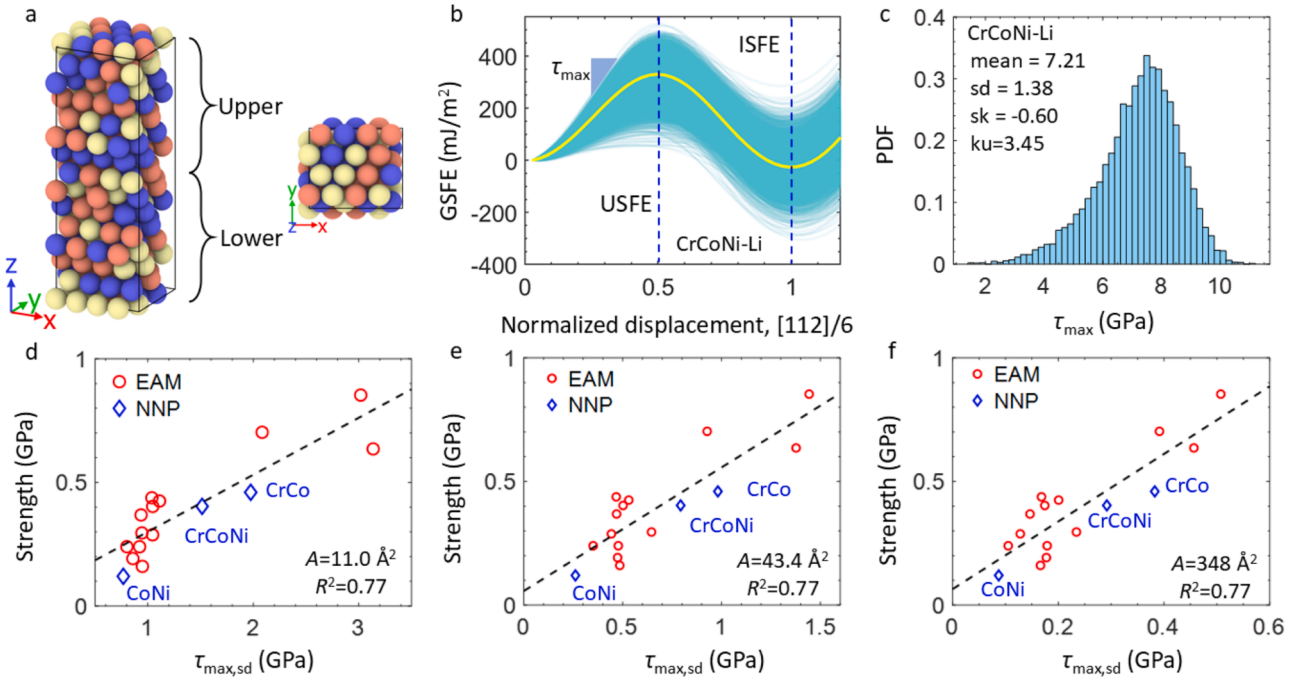

Fig. 6. (a) Configurations used to calculate local-region maximum restoring force (τ_{max}) for CrCoNi-Li. (b) Wide fluctuations of 10,000 GSFE curves. (c) Probability distribution τ_{max}. Correlation between strength and $\tau_{max\text{-}sd}$ for 16 FCC MPEAs using different cross-section area (d) A = 11.0 Å^2, (e) A = 43.4 Å^2 and (f) A = 348 Å^2.

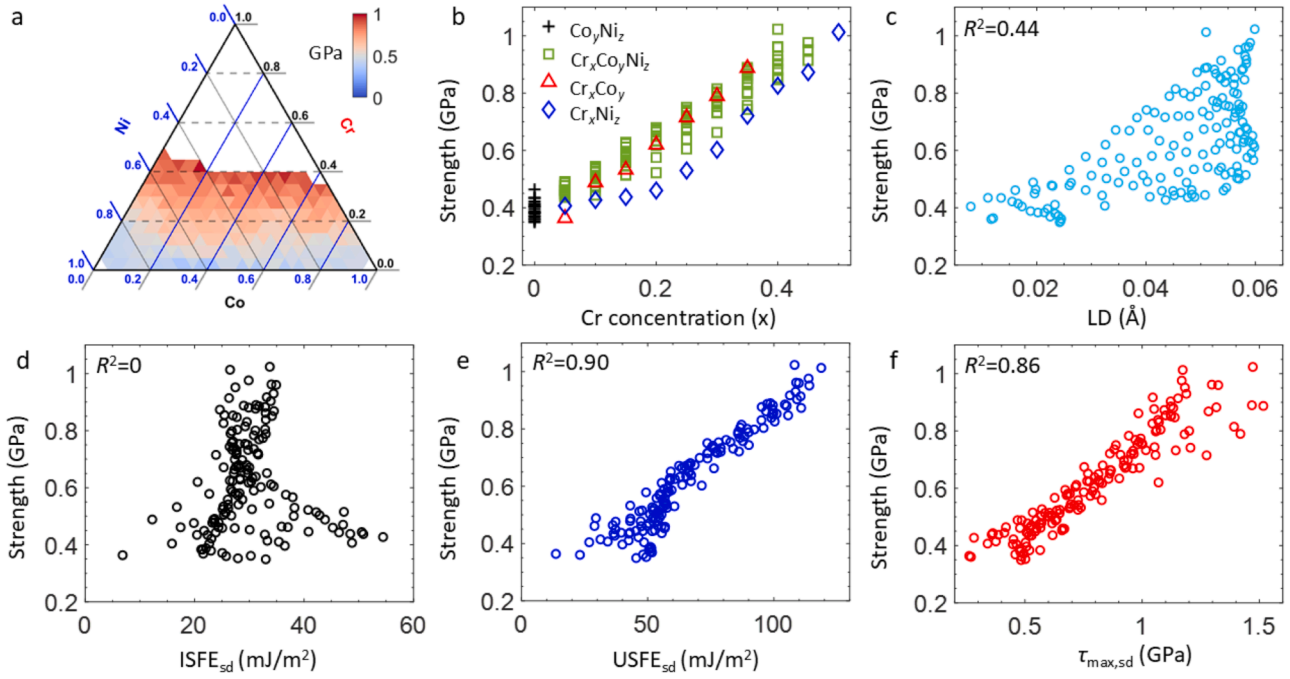

Fig. 7. (a) Strength of all stable $Cr_xCo_yNi_z$ alloys. Relationship between strength and (b) Cr concentration, (c) lattice distortion (LD), (d) standard deviation of ISFE ($ISFE_{sd}$), (e) standard deviation of USFE ($USFE_{sd}$), (f) standard deviation of maximum restoring force ($\tau_{max,sd}$).

for NNP. In fact, it is very challenging to determine potential energy for each atom from DFT because energy contribution from electrons is indistinguishable for different atoms. As a result, the potential energy change as well as $F_{P,sd}$ values for each atom obtained from NNP are merely products of mathematical fitting and lack physical interpretation. On the contrary, here $\tau_{max,sd}$ represents the energy change of the entire supercell in Fig. 6(a), which holds significance in DFT calculations. Therefore, we can conclude that $\tau_{max,sd}$ is the more practical and reliable indicator for predicting the strength of MPEA.

5. Validation by DFT calculations and experiments

In this section, we conduct high-throughput DFT calculations to determine $USFE_{ave}$, $USFE_{sd}$, $\tau_{max,ave}$ and $\tau_{max,sd}$ for 11 MPEAs (CoNi, FeNi, $Ni_{62.5}V_{37.5}$, FeCoNi, MnFeNi, MnCoNi, CrCoNi, VCoNi, MnFeCoNi, CrFeCoNi and CrMnCoNi) and subsequently compare them with the experimentally measured strengths. The experimental data are obtained from Ref [41] at room temperature and Ref [98] at 0 K, which have been utilized to unveil the critical roles of lattice distortion [41] and atomic pressure [98] in the strength of MPEAs. It should be noted that the experimental strengths referenced are the intrinsic strengths of MPEAs,

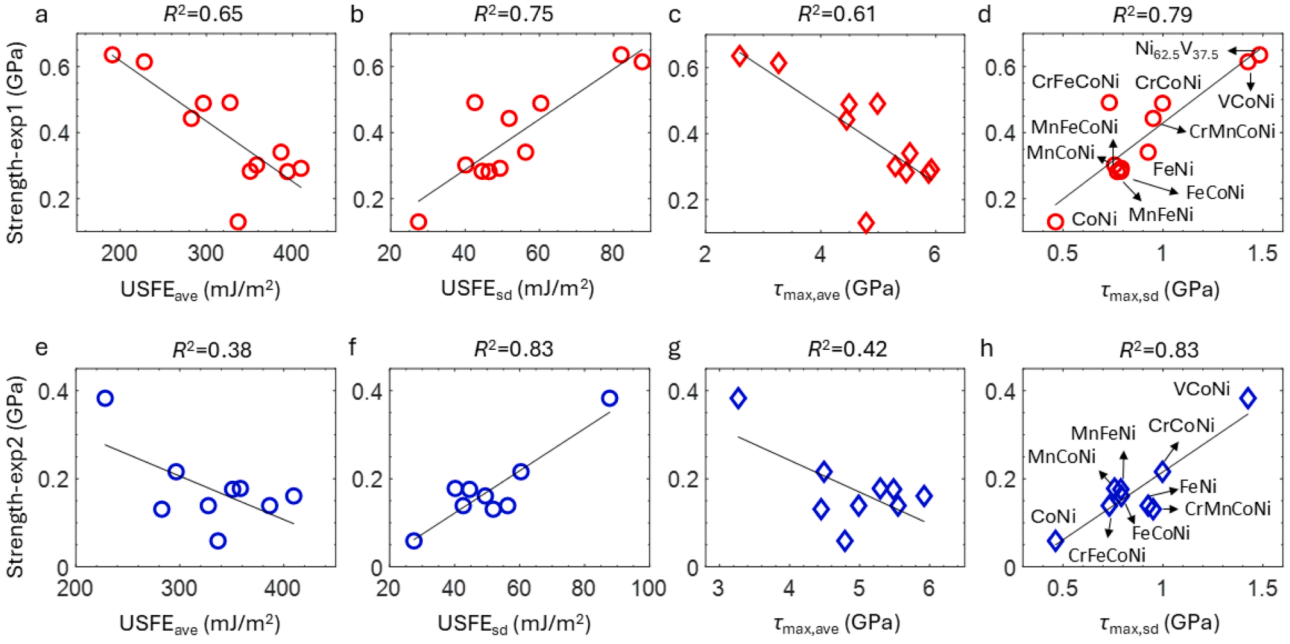

Fig. 8. Relationship between strength of 11 FCC MPEAs from (a-d) experiment data 1 [90,98] at 0 K and (e-h) experiment data 2 at room temperature [41] with respect to $USFE_{ave}$, $USFE_{sd}$, $\tau_{max\text{-}ave}$, and $\tau_{max\text{-}sd}$. Experiment 1 involves data from 11 MPEAs, while experiment 2 includes data from 9 MPEAs.

derived from fitting the Hall-Petch equation to the tensile stress-strain curves of polycrystal samples [41,98], and explicitly exclude contributions from grain boundaries, precipitates, and phase transformations. This ensures a valid comparison with our DFT results. In Figs. 8(a, c, e, g), we observe weak correlations ($R^2 = 0.38\sim0.65$) between $USFE_{ave}$ and $\tau_{max,ave}$ with respect to strength obtained from both experiments. On the contrary, we observe strong correlations ($R^2 = 0.75\sim0.83$) between $USFE_{sd}$ and $\tau_{max,sd}$ with strengths obtained from both experiments, as shown in Fig. 8(b, d, f, h). USFE is closely related to τ_{max} as shown in Fig. 2(b), which explains the similar response of these two fundamental properties to strength. Overall, the comparison between experimental measurements and our DFT calculations aligns with our interatomic potential-based simulations in Section 4, both suggesting that $USFE_{sd}$ and $\tau_{max,sd}$ are effective indicators of intrinsic strength of MPEAs at 0 K and room temperature.

Another significant implication of our findings in Fig. 8 is that $USFE_{ave}$ and $\tau_{max,ave}$ are poorly correlated with the strength of MPEAs. On the contrary, the negative slopes in Fig. 8(a, c, e, g) imply that MPEAs featuring lower $USFE_{ave}$ or $\tau_{max,ave}$ tend to exhibit higher strength. This contradiction to the classical PN model for pure metals suggests that the PN model is not suitable for predicting the intrinsic strength of MPEAs. Despite previous attempts to predict strength using the average properties of MPEAs and the classical PN model [99–102], our findings suggest the inadequacy of this approach. We will employ the simulation results of A-atom potential to further validate this statement in the following section.

6. Stochastic Peierls-Nabarro model

In this section, we delve into the mechanistic origin of the observed strength $\sim \tau_{max,sd}$ by improving the existing SPN model. This is achieved by introducing randomness at the atomic scale into the fundamental properties of the original PN model and integrating it with shearable precipitate model.

6.1. Peierls-Nabarro model in pure systems

First, we discuss the theoretical framework of original PN model and examine its applicability for metals with different material properties. Conceptually, dislocation in crystalline materials can be described by the integro-differential equation, commonly referred to as the PN equation [103]:

$$K\int_{-\infty}^{+\infty}\frac{1}{x-x'}\frac{d\delta(x')}{dx'}dx' = F_b(\delta(x)) \tag{1}$$

where $\delta(x) = \boldsymbol{u}(x,0^+) - \boldsymbol{u}(x,0^-)$ is the slip distribution function ($\boldsymbol{u}(x)$ is the displacement vector at position x in the glide plane), K is the elastic constant which depends on the dislocation type, and F_b is the restoring force defined by GSF surface or curve. The left-hand side of Eq. (1) represents the elastic energy stored within the two elastic half-spaces, whereas the right-hand side quantifies the energy penalty incurred due to misfit across the glide plane. Solving Eq. (1) entails the minimization of the total energy of the dislocation system, encompassing contributions from both elasticity and plasticity. For situations involving wide dislocations, which are commonly encountered in metals, an analytical formula has been provided as follows [94]:

$$\sigma_P = K\frac{b}{a'}\exp\left(-\frac{b}{a'}\frac{K}{2\tau_{max}}\right) \tag{2}$$

where σ_P is the Peierls stress (or lattice friction), a' is the spacing of atomic planes along the line direction when the dislocation is absent, and b is the magnitude of Burgers vector. In FCC metals, $\frac{1}{2}\langle110\rangle$ edge dislocation usually experience dissociation by the following process:

$$\frac{1}{2}\langle110\rangle \rightarrow \frac{1}{6}\langle\bar{1}\bar{1}2\rangle + \frac{1}{6}\langle\bar{2}11\rangle + \mathrm{SF} \tag{3}$$

Assume a is the lattice constant, then the magnitude of the total Burgers vector is $b_t = a\sqrt{2}/2$. Consequently, the magnitude of the Burgers vector (b) in Eq. (2) should be $b_p = b_t\sqrt{3}/3 = a\sqrt{6}/6$ for the leading and trailing partial dislocations. Note that $a' = \frac{\sqrt{2}}{4}a$ for edge dislocation, we have $b_p/a' = 2\sqrt{3}/3$. Although we are working on the edge dislocation with the Burgers vector of $\frac{1}{2}[110]$, the partials have both edge and screw components after dissociation. As a result, the elastic constant is obtained by

$$K = K_s\cos^2\varphi + K_e\sin^2\varphi \tag{4}$$

where $K_s = \mu$ and $K_e = \mu/(1-\nu)$ represent the elastic constants for pure screw and edge dislocations respectively, μ and ν are the isotropic shear modulus and Poisson ratio respectively, and $\varphi = 60^\circ$ for the edge dislocation. Using this simplified PN model, the Peierls stress of pure Ni is estimated as 4.7 MPa, which is close to the result obtained by molecular static simulation [104].

Subsequently, we utilize simulations based on A-atom potentials to investigate the validity of Eq. (2). We generate A-atom potentials for 155 stable compositions of $Cr_xCo_yNi_z$ based on the approach from Ref [31], from which we select 61 compositions characterized by a positive stacking fault energy (SFE). Compositions with a negative SFE, such as equimolar CrCoNi, are excluded due to the instability of edge dislocations and the consequent presence of infinitely long stacking faults. These 61 Aatom potentials represent 61 FCC pure metals with distinct properties, thereby affording us the opportunity to rigorously examine the applicability of Eq. (2) across this diverse dataset. Fig. 9(a) illustrates that the predictions derived from Eq. (2) and the outcomes obtained from A-atom-based atomistic simulations exhibit comparable magnitudes and consistent trend. This observation suggests the potential applicability of Eq. (2). Furthermore, we conduct a comparison between the strength of MPEAs and the strength predicted by A-atom potentials for these 61 compositions, as depicted in Fig. 9(b). Remarkably, the strength of MPEAs is notably higher than that anticipated by A-atom potentials, and no discernible correlation between the two is observed. These findings provide additional evidence indicating that the strength of MPEAs is not solely dictated by the average of their constituent properties, and consequently, the mean-field PN model may not be suitable for accurately predicting the strength of MPEAs.

6.2. Stochastic dislocation mechanics

In MPEAs, the presence of random chemical environments at the atomic scale introduces variability into all fundamental properties. As a consequence, all variables on the right-hand side of Eq. (2) are subjected to spatial fluctuations. In the case of a long dislocation, as illustrated in Fig. 10(a), it can be segmented into shorter segments, each experiencing a distinct atomic environment. Consequently, while the classical PN model remains valid, it is applicable only for each individual short segment. Therefore, Eq. (2) is subjected to randomization and acquires the form:

$$\sigma_{Pi} = K\frac{b_i}{a_i'}\exp\left(-\frac{b_i}{a_i'}\frac{K}{2\tau_{max,i}}\right) \tag{5}$$

where the subscription i denotes the i^{th} segment. The elastic constant K is not subjected to randomization, as the integration on the left side of Eq. (1) spans the entire x dimension, resulting in the influence of only the average K. Eq. (5) suggests that each short segment experiences random local Peierls stress (σ_{Pi}) due to random lattice constant (a) and maximum restoring force (τ_{max}).

In order to determine the overall intrinsic strength of MPEAs, we first follow similar strategy as in Ref [46] to incorporate the Orowan

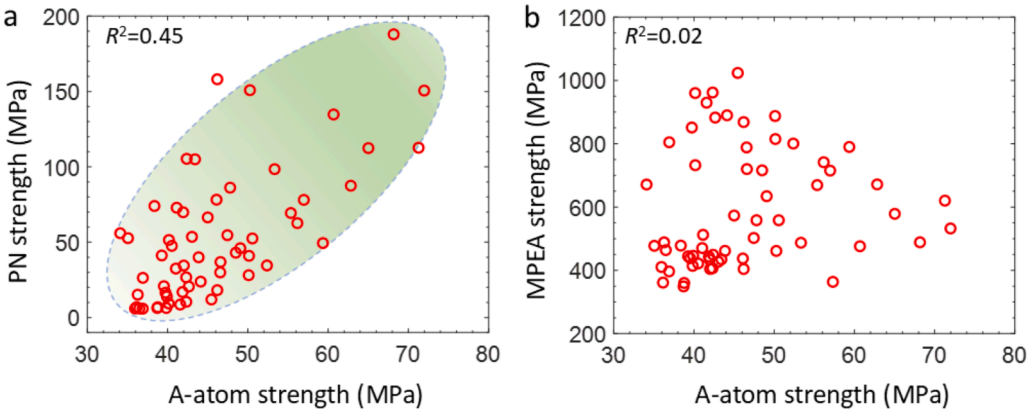

Fig. 9. Scatter plots depicting (a) the strength predicted by Eq. (2) and (b) MPEAs' strength obtained from simulations of CrCoNi-Li, in relation to the simulation results derived from A-atom potential simulations.

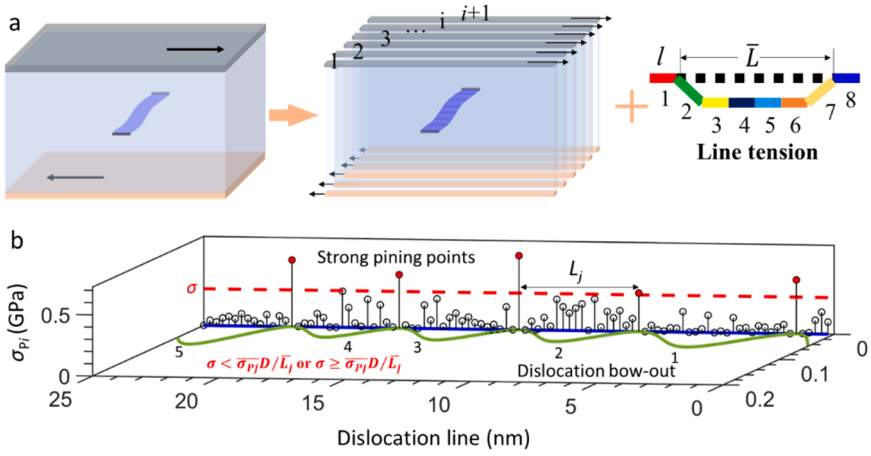

Fig. 10. (a) SPN model by combining random local PN model and line tension model. (b) Schematic representation of dislocation bow out with random local Peierls stress. The dashed red line represents the applied shear stress (σ).

precipitate model which defines the critical stress for a dislocation to bypass a set of "pinning sites":

$$\sigma_c = \frac{\mu b_p}{\overline{L}} \tag{6}$$

where $\overline{L}$ is the average spacing between the pinning sites and σ_c is the critical applied stress. Geometrically, the probability of encountering strong pinning sites satisfying $\sigma_{Pi} > \sigma_c$ should be equal to the ratio of these strong pinning sites to all sites, i.e.,

$$P(\sigma_{Pi} > \sigma_c) = l/\overline{L} \tag{7}$$

where $l = \sqrt{6}a/2$ represents the dislocation length corresponding to the smallest periodicity along the direction of the dislocation line. By combining Eq. (6) and Eq. (7), we can derive an implicit expression for determining the strength of MPEAs (σ_{c1}).

$$P(\sigma_{Pi} > \sigma_{c1}) = 3\frac{\sigma_{c1}}{\mu} \tag{8}$$

While Eq. (8) represents a straightforward model, it utilizes the Orowan precipitate model which assume an impenetrable precipitate. However, dislocation loops due to dislocation bypassing impenetrable precipitates were not observed in previous experiments [19] and atomistic simulations [19,33]. In fact, overcoming random local Peierls barriers during dislocation movement in MPEAs is more akin to cutting through shearable precipitates. As a result, we employ the shearable precipitate hardening model to predict the intrinsic strength of MPEAs [105]:

$$\sigma_c^{sh} = \frac{\overline{\sigma_{Pi}} D}{\overline{L}} \tag{9}$$

where D is precipitate size, and $\overline{\sigma_{Pi}}$ indicates the average of local Peierls stress of strong pining sites i at the given applied stress σ. The intrinsic strength of MPEA (σ_{c2}) in this case can be obtained by:

$$\sigma_{c2} = \frac{\overline{\sigma_{Pj}} D}{\overline{L_j}} \tag{10}$$

In Eq. (10), σ_{Pj} is the local Peierls stress satisfying $\sigma_{Pj} \geq \sigma_{c2}$, which serves as strong pining sites to block the movement of the long dislocation. The dislocation segments corresponding to the sites satisfying $\sigma_{Pi \neq j} < \sigma_{c2}$ are free to bow out. Fig. 10(b) illustrates an exemplary procedure for determining σ_{c2}. When the applied external stress (σ) is small, the majority of pinning points persist as obstacles hindering the motion of the extended dislocation line. The average spacing between these remaining pinning points is very compact, such that $\sigma < \overline{\sigma_{Pj}} D/\overline{L_j}$ and the dislocation cannot move. As σ progressively increases, a greater number of pinning points become ineffective, resulting in fewer obstacles to impede the dislocation's motion. The critical σ is determined when satisfying $\sigma = \overline{\sigma_{Pj}} D/\overline{L_j}$. Therefore, it is evident that the strength of MPEAs is not determined solely by either the strongest or average pinning strength, but rather, the entire distribution of pinning strengths exerts an influence.

7. Solving SPN models using Monte Carlo and symbolic machine learning

7.1. Monte Carlo simulations

Analytically solving SPN models presents significant challenges owing to the incorporation of probability functions for unknown distributions. Consequently, in practical terms, we resort to high-throughput Monte Carlo (MC) simulations. First, we investigate the random distribution of fundamental properties inherent in MPEAs. The statistical distribution of τ_{max} has been investigated in Section 4. Drawing from our simulation outcomes involving 16 MPEAs listed in Table 1 and 155 stable compositions of $Cr_xCo_yNi_z$, it is reasonable to assume that τ_{max} follows a Gaussian distribution, solely characterized by its average ($\tau_{max,ave}$) and standard deviation ($\tau_{max,sd}$). Furthermore, it is important to note that $\tau_{max,sd}$ is dependent on the stacking fault area, as demonstrated in Fig. 6(d-f). We use $\tau_{max,sd}$ calculated based on the minimum stacking fault area ($\sqrt{3}/2a^2$) due to indications from Figs. 3 and 5, which suggest that the pinning sites exhibit comparable small scales. Similarly, we approximate the precipitate size as $D = l$ for the same reason.

Next, we use the atomic displacement (d) of relaxed atoms from their ideal positions in the undistorted crystal lattice to examine the randomness of lattice constant. Fig. 11 (a-c) presents an example analysis of atomic displacement across three dimensions—d_x, d_y, and d_z for CrCoNi-Li—each demonstrating similar Gaussian distribution patterns. We utilize the standard deviation of d_x to characterize the randomness of the lattice constant (a_{sd}), as Eq. (1) solely pertains to one dimension. On the other hand, a_{sd} can be related to LD in MPEAs [37]:

$$LD = \sqrt{\frac{1}{N}\sum_{i}^{N}\left[\left(x_i - x_i'\right)^2 + \left(y_i - y_i'\right)^2 + \left(z_i - z_i'\right)^2\right]} \tag{11}$$

Considering $d_x = x_i - x_i'$, $d_y = y_i - y_i'$, $d_z = z_i - z_i'$, we have $\mathrm{Var}(d_x) = \frac{1}{N}\sum_i^N \left(x_i - x_i'\right)^2$, $\mathrm{Var}(d_y) = \frac{1}{N}\sum_i^N \left(y_i - y_i'\right)^2$, and $\mathrm{Var}(d_z) = \frac{1}{N}\sum_i^N \left(z_i - z_i'\right)^2$. Since $\mathrm{Var}(d_x) = \mathrm{Var}(d_y) = \mathrm{Var}(d_z)$ from Fig. 11 (a-c), we can obtain $LD = \sqrt{3\mathrm{Var}(d_x)} = \sqrt{3}a_{sd}$, indicating that LD is equivalent to the fluctuation of lattice constant.

We then conduct MC simulations, repeating them 10^5 times to solve for σ_{c1} and σ_{c2}, which respectively satisfy Eqs. (8) and (10). We use CrCoNi-Li to illustrate this process. To isolate the individual strengthening effect resulting from lattice distortion, we first set $\tau_{max,sd} = 0$. As depicted in Fig. 12(a), the probability distribution of σ_{Pi} noticeably broadens with increasing values of a_{sd}, yet retains close resemblance to a Gaussian distribution pattern. All values of σ_{Pi} are within the same order of magnitude. For CrCoNi-Li, an a_{sd} value of 0.033 Å results in a minor enhancement in strength for σ_{c1}, while no improvement is observed for σ_{c2}, as depicted in Fig. 12(b). Fig. 12(c) reveals the linear relationship between σ_{c1} and increasing a_{sd} values. Remarkably, despite a significant lattice distortion ($a_{sd} = 0.025a$), only a marginal enhancement (from 40 MPa to 75 MPa) is observed for σ_{c1}, while no enhancement is noted for σ_{c2}. These results suggest that lattice distortion alone has a limited strengthening effect on MPEAs. Similarly, we set $a_{sd} = 0$ and investigate the strengthening effect of $\tau_{max,sd}$. In contrast to lattice constant, τ_{max} exhibits significantly larger fluctuations, as depicted in Fig. 6, due to the combined effects of random chemical elements and lattice distortion, amplifying the inherent randomness. It is observed that different values of $\tau_{max,sd}$ significantly alter the distribution pattern of σ_{Pi}, transitioning it from a Gaussian-like distribution ($\alpha = \tau_{max,sd}/\tau_{max,ave} = 0.01$) to an exponential-like distribution ($\alpha = \tau_{max,sd}/\tau_{max,ave} \geq 0.1$) as illustrated in Fig. 12(d). This is due to the combined effects of highly nonlinear exponential function in original PN equation and large $\tau_{max,sd}$. The consequence of the transition in the distribution pattern of σ_{Pi} is the emergence of more weaker and stronger pinning sites for larger $\tau_{max,sd}$. When $\tau_{max,sd} = 0.5\tau_{max}$, there are large amount of strong pining sites with local σ_{Pi} exceeding 1.0 GPa, which can significantly increase the strength of MPEAs. For CrCoNi-Li, $\tau_{max,sd} = 3.02$ GPa $= 0.42\tau_{max,ave}$ leads to $\sigma_{c1} = 1.1$ GPa and $\sigma_{c2} = 256.1$ MPa as shown in Fig. 12(e). Comparing these results with our simulation findings for CrCoNi-Li in Fig. 4 (853.4 MPa), it becomes evident that σ_{c1} overestimates the strength due to the utilization of impenetrable precipitates in the dislocation line tension model. Conversely, σ_{c2} underestimates the strength, implying that other strengthening mechanisms, such as stacking-fault-energy fluctuation, also contribute to the strength. The underestimation of σ_{c2} may also be attributed to inaccuracies in $\tau_{max,sd}$, which can be improved in the future work. Nevertheless, we calculate σ_{c1} and σ_{c2} using different $\tau_{max,sd}$ and the resulting plot (Fig. 12(f)) demonstrates that both σ_{c1} and σ_{c2} show a linear relationship with $\tau_{max,sd}$, demonstrating the dominant role of $\tau_{max,sd}$ in MPEAs' strength. These findings thus align with our simulation results presented in Sections 4 and 5.

7.2. Symbolic machine learning: SISSO

Finally, we utilize an advanced symbolic machine learning model, Sure Independence Screening and Sparsifying Operator (SISSO) [106], to derive interpretable and analytical models capable of predicting the intrinsic strength of MPEAs based on K, μ, $\tau_{max,ave}$ and $\tau_{max,sd}$. These parameters are considered because they are the sole influencing factors in SPN models. SISSO facilitates the creation of extensive feature spaces by synthesizing primary features using designated operators. It employs Sure Independent Screening to identify optimal subsets of features [107], in conjunction with sparse operators like the Least-Absolute Shrinkage and Selection Operator (LASSO) and l_0-norm regularized minimization techniques [108]. Consequently, SISSO enables the development of analytical models that may offer greater interpretability and transferability compared to conventional machine learning approaches. To prepare a comprehensive dataset for training, we employ MC simulations to calculate intrinsic strength (σ_{c2}) of MPEAs for a large

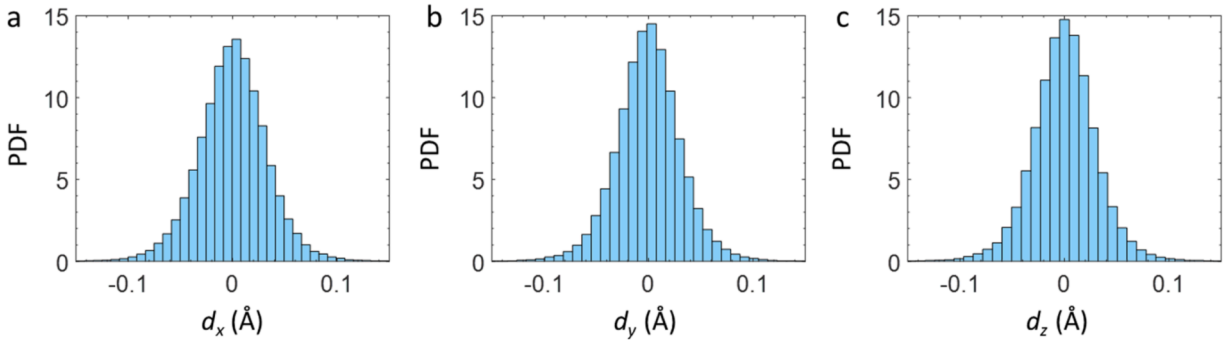

Fig. 11. Statistical distribution of lattice constant in CrCoNi-Li at three directions.

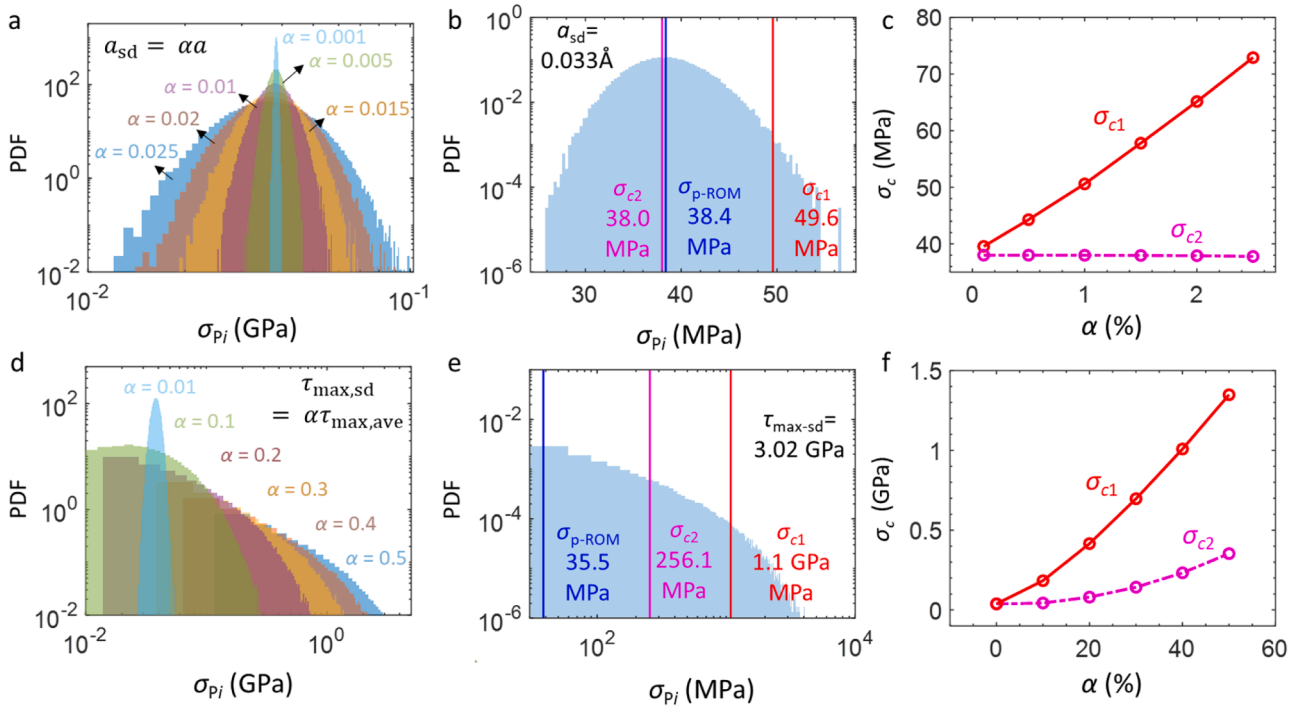

Fig. 12. Probability distribution of local Peierls stress (σ_{Pi}) with different (a) lattice distortion (a_{sd}) and (d) $\tau_{max,sd}$. Intrinsic strength of CrCoNi-Ni due to (b) a_{sd} and (e) $\tau_{max,sd}$. The variation in intrinsic strength with respect to (c) a_{sd} and (f) $\tau_{max,sd}$. $\alpha = a_{sd}/a$ and $\alpha = \tau_{max,sd}/\tau_{max,ave}$ in (c) and (f).

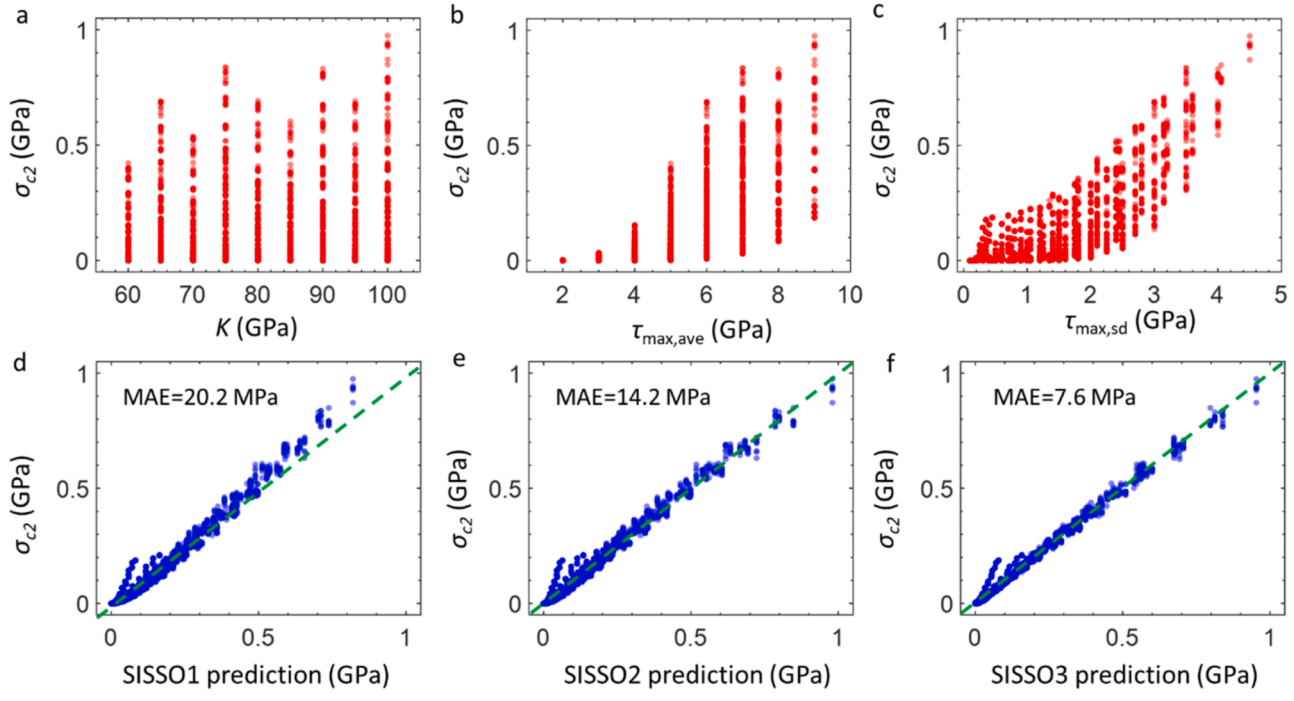

Fig. 13. (a-c) Parametric study of MPEAs' strength with respect to K, $\tau_{max,ave}$ and $\tau_{max,sd}$. (d-f) Performance of the three SISSO models.

range of parameter set: $K \in [60, 100]$ GPa, $\mu \in [45, 75]$ GPa, $\tau_{max,ave} \in [2, 10]$ GPa and $\tau_{max,sd} \in [0, 0.5]\tau_{max,ave}$. Fig. 13(a-c) demonstrate that K exhibits no systematic influence on σ_{c2}, whereas σ_{c2} increases with $\tau_{max,ave}$ and $\tau_{max,sd}$. In SISSO, four material properties ($[K, \mu, \tau_{max,ave}, \tau_{max,sd}]$) and four operators [×, /, ^2, ^3, exp(-)] are used to construct features. We obtain three SISSO models, each trained on the generated dataset but varying in complexity and accuracy as shown below:

$$\text{SISSO1} = 250\tau_{max,sd}\left(\frac{\tau_{max,ave}}{K}\right)^3 \tag{12}$$

$$\text{SISSO2} = 181.88\tau_{max,sd}\left(\frac{\tau_{max,ave}}{K}\right)^3 + 288.46\tau_{max,sd}^2\left(\frac{\tau_{max,ave}}{K}\right)^4 \tag{13}$$

$$\mathrm{SISSO3} = \left| \begin{array}{l} 460.29\tau_{\max,\mathrm{sd}}\left(\frac{\tau_{\max,\mathrm{ave}}}{K}\right)^3 - 19.8\tau_{\max,\mathrm{sd}}\left(\frac{\tau_{\max,\mathrm{ave}}}{K}\right)^2 \\ \quad + 13.07\frac{\tau_{\max,\mathrm{sd}}^6}{K\tau_{\max,\mathrm{ave}}^4} \end{array} \right| \tag{14}$$

It is important to note that during the SISSO training process, the shear modulus μ is disregarded, with only K, $\tau_{\max,\mathrm{ave}}$, and $\tau_{\max,\mathrm{sd}}$ considered as the influencing factors. Fig. 13(d-f) illustrate that these models accurately predict the intrinsic strength of MPEAs. Moreover, all the three models indicate that the intrinsic strengths of MPEA are dominated by linear term of $\tau_{\max,\mathrm{sd}}$, which aligns with our simulations and comparison with the experiments. Interestingly, $\tau_{\max,\mathrm{sd}}$ and $\frac{\tau_{\max,\mathrm{ave}}}{K}$ serve as two fundamental units for constructing SISSO models. $\tau_{\max,\mathrm{ave}}/K$ represents the effects of average properties which can be estimated by ROM, and the value is bounded by the constituent elements. As a result, $\tau_{\max,\mathrm{ave}}/K$ has limited effects on MPEAs' strength, while $\tau_{\max,\mathrm{sd}}$ represents the random effect and dominates the strength of MPEAs.

The current SPN models demonstrate the ability to reproduce the linear relationship between $\tau_{\max,\mathrm{sd}}$ and the intrinsic strength of MPEAs, indicating that the analytical model in Eq. (2) effectively captures the dominant physics governing the Peierls stress in materials. However, our simulation results in Fig. 9 reveal that this simplified PN model lacks accuracy. In fact, Eq. (2) is typically employed to estimate the order of magnitude of Peierls stress. The prevailing approach for predicting PN stress involves using more accurate PN models, such as the semidiscrete variational Peierls-Nabarro (SVPN) model [109], which incorporates the entire GSFE surface. This can be explored in our future work by substituting Eq. (5) with a random SVPN model. High-throughput MC simulations and symbolic machine learning can be then used to derive more accurate physical models to predict the strength of MPEAs. On the other hand, the current SPN model does not incorporate the effect of SRO, which is believed to significantly influence the intrinsic properties of MPEAs. However, our SPN model can be readily extended to include the SRO effect by considering the additional strengthening effect due to SRO in the precipitate hardening model. Finally, although BCC MPEAs with edge dislocations are not included in our approach, we expect their strengths to exhibit similar trends to those of FCC MPEAs, like the SSS model.

8. Discussion

In contrast to the solid solute-induced strength in the SSS model, we designate it as the effective lattice friction of MPEAs within the framework of SPN. This terminology aligns with the notion of regular lattice friction defined in pure metals. It represents the intrinsic strength of the materials, excluding contributions from other microstructures such as vacancies, precipitates, and grain/phase boundaries [40,41]. Compared to the SSS model, the proposed SPN models offer several advantages. First, the SPN models explicitly consider the interaction between solute atoms and the dislocation core, a natural advantage inherent in the PN model. In contrast, SSS models only account for interactions between solute atoms and the dislocation based on elastic interactions associated with atomic size misfit and modulus misfit of the solute atom. Second, DFT calculations of elastic constants, GSFE or $\tau_{\max}$ have become common practice for MPEAs [95,110], requiring small configurations that capture fluctuations as comprehensively as possible. This facilitates the assessment of accurate SPN models with ease. Moreover, it is possible to employ ROM to estimate elastic constant, average and standard deviation of $\tau_{\max}$, enabling the fast screening of MPEAs' strength with reasonable accuracy. For SSS models, however, the solute/dislocation interaction energies in the full model are prohibitive for DFT calculations, whereas misfit volume values in the simplified model are less common [23]. Third, the SPN model treats the intrinsic strength of MPEAs as effective lattice friction, a concept analogous to its counterpart in pure metals. It is evident that MPEAs exhibit lattice friction one order of magnitude higher than their constituent elements, fundamentally challenging the assumptions of the ROM approach. The SPN model provides a comprehensive explanation for this phenomenon, thereby enriching our understanding of MPEAs and addressing various related problems. Lastly, our SPN model is robustly designed to seamlessly incorporate the effects of SRO by accounting for variations in precipitate sizes dictated by SRO. Building on this framework, it is reasonable to postulate that the emergence of SRO mitigates the inherent randomness in MPEAs, thereby subtly attenuating their intrinsic strengthening mechanisms. Conversely, SRO manifests as disproportionately larger precipitates compared to the typical, randomly distributed pinning points in random solid solution MPEAs, which substantially augments precipitate hardening. This sophisticated dual influence of SRO on the intrinsic strength of MPEAs has been substantiated by sophisticated theoretical models [30] and detailed atomistic simulations [111], underscoring the comprehensive capability of our SPN model to predict and analyze these complex phenomena.

On the other hand, it is important to note that the current SPN model is limited to scenarios at 0 K, where effects of temperature and strain rate are not considered. Our model does not account for the critical quantity, the dislocation glide energy barrier. In contrast, the model proposed by Varvenne and Curtin [24] incorporates these factors. They provide an expression for the finite-temperature, finite-strain-rate yield stress as follows:

$$\sigma(T,\dot{\varepsilon}) = \sigma_c\left[1 - \left(\frac{k_\mathrm{B}T}{\Delta E_b}\ln\frac{\dot{\varepsilon}_0}{\dot{\varepsilon}}\right)^{2/3}\right] \tag{15}$$

where σ_c is the intrinsic strength at 0 K, T denotes temperature, $\dot{\varepsilon}$ is the strain rate, $\dot{\varepsilon}_0$ is the reference strain rate, k_B is the Boltzmann constant, and ΔE_b is the dislocation glide energy barrier. To determine the intrinsic strength at finite temperatures, one can employ Eq. (15). Further details on determiningΔE_b can be obtained from Ref [24]. The direct determination of ΔE_b from fundamental properties, such as GSFE and elastic constants, will be the focus of our future work.

A crucial implication of this work is understanding the circumstances and reasons behind the failure of ROM in predicting the behavior of MPEAs. ROM has traditionally been utilized to predict a range of properties in alloys and MPEAs, including lattice constant [112,113], misfit volume [24], elastic properties [114], and thermal expansion [115]. Interestingly, we find that surface energy and unstable stacking fault energy in BCC MPEAs also adhere to ROM predictions using results of recent DFT calculations [93]. Although ROM may not accurately predict certain properties such as elastic properties [112,114], surface energy, and unstable stacking fault energy [93], the deviations from actual values are relatively small. This suggests that these fundamental properties of MPEAs are bounded by the properties of their constituent elements. On the other hand, A-atom potential model is an extension of ROM, but in this model, all properties are concentration-weighted at the potential level [31]. Consequently, A-atom potential can be utilized to predict the average properties of MPEAs with less effort, including elastic constants, surface energy, stacking fault energy, and even dislocation width. However, A-atom potential cannot reproduce the correct critical stress for dislocation glide in MPEAs, which is also observed in our results (Fig. 9(a)) and discussed in Ref [24]. This suggests that the intrinsic strength of MPEAs is not bounded by the individual strength of their constituent elements, underscoring potential limitations of ROM and ROM-based or mean-field PN models in predicting these properties.

Our research elucidates the mechanistic origin underlying the breakdown of ROM in determining the strength of MPEAs. This is known as the widely recognized cocktail effect in MPEAs. This breakdown of ROM is attributed to the highly nonlinear exponential function within the PN model (Eq. (2)) and substantial fluctuations in GSFE or $\tau_{\max}$. Specifically, the exponential function can significantly amplify $\tau_{\max}$ fluctuations, leading to a considerable increase in local Peierls stress

spanning several orders of magnitude (Fig. 12(d)). For the same reason, we anticipate that high-entropy covalent materials such as high-entropy ceramics will have insignificant strength improvement since the PN model takes form [116]:

$$\sigma_P = 4\frac{\tau_{max}^2}{K} \tag{16}$$

where the square function does not significantly alter the probability distribution of σ_P away from the distribution of τ_{max}. Overall, we conclude that although ROM applies to the fundamental properties of MPEAs, it fails to predict macroscopic behaviors that exhibit highly nonlinear relationships with these fundamental properties at the atomic scale. It is only under these conditions that the cocktail effect in MPEAs can emerge.

Another relevant example involves hydrogen or vacancy diffusion in MPEAs, where the exponential function also emerges in the basic Arrhenius equation for the local diffusion behavior:

$$D = D_0 \exp\left(-\frac{\Delta E}{k_B T}\right) \tag{17}$$

where D_0 is the characteristic diffusivity when temperature goes to infinite, ΔE is the diffusion barrier, k_B is the Boltzmann constant, T is the temperature. Although this model aptly describes individual atomic movements, it fails to capture the more complex, collective diffusion behaviors observed on a macroscopic scale in MPEAs. The well-documented phenomenon of sluggish diffusion, extensively observed in prior studies, indicates that diffusion within MPEAs is not confined to the traditional behavior observed in individual elemental systems. In fact, diffusion in MPEAs is not merely a function of one or two migrations barriers (ΔE) but is significantly influenced by the alloy's heterogeneous composition [117–119]. This heterogeneity leads to a variation in local microenvironments, which in turn cause the fluctuations of ΔE at the atomic scale [120–122]. Consequently, we expect that the statistics of ΔE (such as ΔE_{ave} and ΔE_{sd}) dominates the overall diffusion behavior in MPEAs. This aligns with a recent kinetic Monte Carlo study showing that in FCC CoNiFeCrMn, vacancy diffusivity is determined by the standard deviations of site energies and migration barriers [121].

Last but not least, this research underscores the critical implications of employing EAM potentials for researching MPEAs. Our findings reveal that although ROM-based and DFT-fitted EAM potentials may not capture the exact properties of real materials, they consistently exhibit internal coherence. This consistent behavior underscores the value of EAM potentials in deciphering the complex deformation mechanisms inherent in MPEAs. Crucially, we establish that the linear relationship identified between the strength of MPEAs and $\tau_{max,sd}$ derived from EAM simulations is robust and transferable to materials synthesized experimentally. This discovery not only enhances our understanding of MPEA mechanics but also sets a new benchmark for predictive materials modeling. In contrast, despite the widespread use of MLIPs in MPEA studies [67,84,123,124], their application demands careful scrutiny. MLIPs inherently lack a physical foundation [125], except for those that are physics-informed [126,127]. At its core, an MLIP represents a combination of optimized hyperparameters that have been fitted using DFT data. To ensure MLIPs are effective in specific applications, it is crucial that they are meticulously trained with relevant, high-quality DFT data. However, validating MLIPs for systems containing more than 1000 atoms presents a significant challenge, primarily due to the size limitations inherent in DFT calculations. This challenge necessitates a cautious approach to the interpretation and application of MLIPs, especially when dealing with large-scale complex behaviors. Our findings presented in Fig. 5 exemplify such a case.

9. Conclusions

In conclusion, this work has employed a comprehensive approach, combining interatomic potential-based large-scale atomistic simulations, high-throughput DFT calculations, the Stochastic Peierls-Nabarro (SPN) model, and symbolic machine learning, to explore the mechanistic origin of the exceptional intrinsic strength of multi-principal element alloys (MPEAs). The main conclusions are:

- The standard deviation of atomic pinning point strength effectively characterizes the intrinsic strength of MPEAs across all examined EAM potentials, except for NNP.
- The linear dependence of the standard deviation of maximum restoring force ($\tau_{max,sd}$) on the intrinsic strength of MPEAs is revealed across various interatomic potentials. This relationship is further highlighted through a comparison between DFT calculations and experimental data.
- SPN models are developed by incorporating both the τ_{max}-dependent PN model and a shearable precipitate model, and subsequently solved using Monte Carlo simulations.
- It is revealed that the remarkable intrinsic strength of MPEAs stems from the presence of highly nonlinear exponential functions within the PN model, coupled with significant fluctuations in τ_{max}.
- Analytical models for the intrinsic strength of MPEAs are formulated through symbolic machine learning techniques, demonstrating strong agreement with our simulation results.
- While EAM potentials may not accurately calculate the properties of real materials like DFT, their inherent coherence and remarkable computational efficiency make them a powerful tool for unraveling the intricate mechanisms within MPEAs.

CRediT authorship contribution statement

Fei Shuang: Writing – review & editing, Writing – original draft, Validation, Methodology, Data curation, Conceptualization. **Luca Laurenti:** Writing – review & editing, Supervision, Methodology, Funding acquisition. **Poulumi Dey:** Writing – review & editing, Supervision, Methodology, Funding acquisition, Conceptualization.

Declaration of competing interest

The authors declare that they have no known competing financial interests or personal relationships that could have appeared to influence the work reported in this paper.

Acknowledgments

This work was sponsored by Nederlandse Organisatie voor WetenschappelijkOnderzoek (The Netherlands Organization for Scientific Research, NWO) domain Science for the use of supercomputer facilities. The authors acknowledge the use of DelftBlue supercomputer, provided by Delft High Performance Computing Center (https://www.tudelft.nl/dhpc). The authors are grateful to the reviewers for their insightful and constructive suggestions.

References

[1] W. Li, D. Xie, D. Li, Y. Zhang, Y. Gao, P.K. Liaw, Mechanical behavior of high-entropy alloys, Prog. Mater. Sci. 118 (2021) 100777, https://doi.org/10.1016/j.pmatsci.2021.100777.
[2] E.P. George, W.A. Curtin, C.C. Tasan, High entropy alloys: a focused review of mechanical properties and deformation mechanisms, Acta Mater. 188 (2020) 435–474, https://doi.org/10.1016/j.actamat.2019.12.015.
[3] Z. Li, S. Zhao, R.O. Ritchie, M.A. Meyers, Mechanical properties of high-entropy alloys with emphasis on face-centered cubic alloys, Prog. Mater. Sci. 102 (2019) 296–345, https://doi.org/10.1016/j.pmatsci.2018.12.003.
[4] Y. Xu, X. Lu, X. Yang, W. Li, Z. Aitken, G. Vastola, H. Gao, Y.-W. Zhang, Temperature-dependent, multi-mechanism crystal plasticity reveals the deformation and failure behaviour of multi-principal element alloys, J. Mech. Phys. Solids. 185 (2024) 105549, https://doi.org/10.1016/j.jmps.2024.105549.
[5] M.A. Khan, M. Hamza, J. Brechtl, Z. Nazir, N.A. Qaisrani, G. Yasin, T. Ahmad, W. B. Liao, P.K. Liaw, M.A. Afifi, Development and characterization of a low-density

TiNbZrAlTa refractory high entropy alloy with enhanced compressive strength and plasticity, Mater. Charact. 205 (2023) 113301, https://doi.org/10.1016/J.MATCHAR.2023.113301.
[6] L. Zhang, R. Huang, F. Zhou, A. Amar, H. Yan, Y. Zhang, Y. Lu, Remarkable improved strength and ductility in brittle eutectic high-entropy alloy via a novel spheroidization and recrystallization strategy, J. Mater. Sci. Technol. 187 (2024) 177–187, https://doi.org/10.1016/J.JMST.2023.11.050.
[7] S.A.A. Shams, J.W. Bae, J.N. Kim, H.S. Kim, T. Lee, C.S. Lee, Origin of superior low-cycle fatigue resistance of an interstitial metastable high-entropy alloy, J. Mater. Sci. Technol. 115 (2022) 115–128, https://doi.org/10.1016/J.JMST.2021.10.010.
[8] Y. Qiu, S. Thomas, M.A. Gibson, H.L. Fraser, N. Birbilis, Corrosion of high entropy alloys, Npj. Mater. Degrad. 1 (1) (2017) 1–18, https://doi.org/10.1038/s41529-017-0009-y, 12017.
[9] Y. Shi, B. Yang, P. Liaw, Corrosion-Resistant High-Entropy Alloys: a Review, Metals. (Basel) 7 (2017) 43, https://doi.org/10.3390/met7020043.
[10] H. Luo, W. Lu, X. Fang, D. Ponge, Z. Li, D. Raabe, Beating hydrogen with its own weapon: nano-twin gradients enhance embrittlement resistance of a high-entropy alloy, Materials Today 21 (2018) 1003–1009, https://doi.org/10.1016/j.mattod.2018.07.015.
[11] H. Luo, S.S. Sohn, W. Lu, L. Li, X. Li, C.K. Soundararajan, W. Krieger, Z. Li, D. Raabe, A strong and ductile medium-entropy alloy resists hydrogen embrittlement and corrosion, Nat. Commun. 11 (1) (2020) 1–8, https://doi.org/10.1038/s41467-020-16791-8, 202011.
[12] A.M.Z. Tan, Z. Li, Y. Zhao, U. Ramamurty, H. Gao, Modeling the improved hydrogen embrittlement tolerance of twin boundaries in face-centered cubic complex concentrated alloys, J. Mech. Phys. Solids. (2024) 105657, https://doi.org/10.1016/j.jmps.2024.105657.
[13] O. El Atwani, H.T. Vo, M.A. Tunes, C. Lee, A. Alvarado, N. Krienke, J. D. Poplawsky, A.A. Kohnert, J. Gigax, W.Y. Chen, M. Li, Y.Q. Wang, J.S. Wróbel, D. Nguyen-Manh, J.K.S. Baldwin, O.U. Tukac, E. Aydogan, S. Fensin, E. Martinez, A quinary WTaCrVHf nanocrystalline refractory high-entropy alloy withholding extreme irradiation environments, Nat. Commun. 14 (1) (2023) 1–12, https://doi.org/10.1038/s41467-023-38000-y, 202314.
[14] O. El-Atwani, N. Li, M. Li, A. Devaraj, J.K.S. Baldwin, M.M. Schneider, D. Sobieraj, J.S. Wróbel, D. Nguyen-Manh, S.A. Maloy, E. Martinez, Outstanding radiation resistance of tungsten-based high-entropy alloys, Sci. Adv. 5 (2019), https://doi.org/10.1126/sciadv.aav2002.
[15] Z. Li, K.G. Pradeep, Y. Deng, D. Raabe, C.C. Tasan, Metastable high-entropy dual-phase alloys overcome the strength–ductility trade-off, Nature 534 (7606) (2016) 227–230, https://doi.org/10.1038/nature17981, 2016534.
[16] E. Ma, X. Wu, Tailoring heterogeneities in high-entropy alloys to promote strength–ductility synergy, Nat. Commun. 10 (1) (2019) 1–10, https://doi.org/10.1038/s41467-019-13311-1, 201910.
[17] E. Mak, B. Yin, W.A. Curtin, A ductility criterion for bcc high entropy alloys, J. Mech. Phys. Solids. 152 (2021) 104389, https://doi.org/10.1016/j.jmps.2021.104389.
[18] D. Liu, Q. Yu, S. Kabra, M. Jiang, P. Forna-Kreutzer, R. Zhang, M. Payne, F. Walsh, B. Gludovatz, M. Asta, A.M. Minor, E.P. George, R.O. Ritchie, Exceptional fracture toughness of CrCoNi-based medium- and high-entropy alloys at 20 kelvin, Science (1979) 378 (2022) 978–983, https://doi.org/10.1126/science.abp8070, 1979.
[19] D. Utt, S. Lee, Y. Xing, H. Jeong, A. Stukowski, S.H. Oh, G. Dehm, K. Albe, The origin of jerky dislocation motion in high-entropy alloys, Nat. Commun. 13 (2022) 4777, https://doi.org/10.1038/s41467-022-32134-1.
[20] F. Zhao, W. Liu, X. Yi, Y. Zhang, H. Duan, Multiscale modeling of dislocation-mediated plasticity of refractory high entropy alloys, J. Mech. Phys. Solids. 187 (2024) 105640, https://doi.org/10.1016/j.jmps.2024.105640.
[21] R. Labusch, A Statistical Theory of Solid Solution Hardening, Physica Status Solidi (b) 41 (1970) 659–669, https://doi.org/10.1002/pssb.19700410221.
[22] I. Toda-Caraballo, P.E.J. Rivera-Díaz-del-Castillo, Modelling solid solution hardening in high entropy alloys, Acta Mater. 85 (2015) 14–23, https://doi.org/10.1016/j.actamat.2014.11.014.
[23] C.R. LaRosa, M. Shih, C. Varvenne, M. Ghazisaeidi, Solid solution strengthening theories of high-entropy alloys, Mater. Charact. 151 (2019) 310–317, https://doi.org/10.1016/j.matchar.2019.02.034.
[24] C. Varvenne, A. Luque, W.A. Curtin, Theory of strengthening in fcc high entropy alloys, Acta Mater. 118 (2016) 164–176, https://doi.org/10.1016/j.actamat.2016.07.040.
[25] C. Varvenne, G.P.M. Leyson, M. Ghazisaeidi, W.A. Curtin, Solute strengthening in random alloys, Acta Mater. 124 (2017) 660–683, https://doi.org/10.1016/j.actamat.2016.09.046.
[26] R.E. Kubilay, W.A. Curtin, Theory of twin strengthening in fcc high entropy alloys, Acta Mater. 216 (2021) 117119, https://doi.org/10.1016/j.actamat.2021.117119.
[27] F. Maresca, W.A. Curtin, Mechanistic origin of high strength in refractory BCC high entropy alloys up to 1900K, Acta Mater. 182 (2020) 235–249, https://doi.org/10.1016/j.actamat.2019.10.015.
[28] F. Maresca, W.A. Curtin, Theory of screw dislocation strengthening in random BCC alloys from dilute to “High-Entropy” alloys, Acta Mater. 182 (2020) 144–162, https://doi.org/10.1016/j.actamat.2019.10.007.
[29] A. Tehranchi, B. Yin, W.A. Curtin, Solute strengthening of basal slip in Mg alloys, Acta Mater. 151 (2018) 56–66, https://doi.org/10.1016/j.actamat.2018.02.056.
[30] S. Nag, W.A. Curtin, Solute-strengthening in metal alloys with short-range order, Acta Mater. 263 (2024) 119472, https://doi.org/10.1016/j.actamat.2023.119472.
[31] C. Varvenne, A. Luque, W.G. Nöhring, W.A. Curtin, Average-atom interatomic potential for random alloys, Phys. Rev. B 93 (2016) 104201, https://doi.org/10.1103/PhysRevB.93.104201.
[32] A. Ghafarollahi, F. Maresca, W. Curtin, Solute/screw dislocation interaction energy parameter for strengthening in bcc dilute to high entropy alloys, Model. Simul. Mat. Sci. Eng. 27 (2019) 085011, https://doi.org/10.1088/1361-651X/ab4969.
[33] Q.-J. Li, H. Sheng, E. Ma, Strengthening in multi-principal element alloys with local-chemical-order roughened dislocation pathways, Nat. Commun. 10 (2019) 3563, https://doi.org/10.1038/s41467-019-11464-7.
[34] K. Chu, E. Antillon, C. Stewart, K. Knipling, P. Callahan, S. Wu, D. Rowenhorst, D. L. McDowell, Investigation of chemical short range order strengthening in a model Fe–12Ni–18Cr (at. %) stainless steel alloy: a modeling and experimental study, Acta Mater. 261 (2023) 119385, https://doi.org/10.1016/j.actamat.2023.119385.
[35] Z. Pei, M. Eisenbach, P.K. Liaw, M. Chen, Nanoscale fluctuation of stacking fault energy strengthens multi-principal element alloys, J. Mater. Sci. Technol. 158 (2023) 218–225, https://doi.org/10.1016/j.jmst.2023.01.042.
[36] G. Huang, X. Zhang, R. Zhang, W.-R. Jian, X. Zou, K. Wang, Z. Xie, X. Yao, The shear softening and dislocation glide competition due to the shear-induced short-range order degeneration in CoCrNi medium-entropy alloy, J. Mater. Sci. Technol. 192 (2024) 108–122, https://doi.org/10.1016/j.jmst.2023.12.024.
[37] C. Tandoc, Y.-J. Hu, L. Qi, P.K. Liaw, Mining of lattice distortion, strength, and intrinsic ductility of refractory high entropy alloys, NPJ. Comput. Mater. 9 (2023) 53, https://doi.org/10.1038/s41524-023-00993-x.
[38] A. Roy, P. Sreeramagiri, T. Babuska, B. Krick, P.K. Ray, G. Balasubramanian, Lattice distortion as an estimator of solid solution strengthening in high-entropy alloys, Mater. Charact. 172 (2021) 110877, https://doi.org/10.1016/j.matchar.2021.110877.
[39] P. Thirathipviwat, S. Sato, G. Song, J. Bednarcik, K. Nielsch, J. Jung, J. Han, A role of atomic size misfit in lattice distortion and solid solution strengthening of TiNbHfTaZr high entropy alloy system, Scr. Mater. 210 (2022) 114470, https://doi.org/10.1016/j.scriptamat.2021.114470.
[40] Y.Y. Zhao, Z.F. Lei, Z.P. Lu, J.C. Huang, T.G. Nieh, A simplified model connecting lattice distortion with friction stress of Nb-based equiatomic high-entropy alloys, Mater. Res. Lett. 7 (2019) 340–346, https://doi.org/10.1080/21663831.2019.1610105.
[41] S.S. Sohn, A. Kwiatkowski da Silva, Y. Ikeda, F. Körmann, W. Lu, W.S. Choi, B. Gault, D. Ponge, J. Neugebauer, D. Raabe, Ultrastrong Medium-Entropy Single-Phase Alloys Designed via Severe Lattice Distortion, Advanced Materials 31 (2019) 1807142, https://doi.org/10.1002/adma.201807142.
[42] N.L. Okamoto, K. Yuge, K. Tanaka, H. Inui, E.P. George, Atomic displacement in the CrMnFeCoNi high-entropy alloy - A scaling factor to predict solid solution strengthening, AIP. Adv. 6 (2016) 125008, https://doi.org/10.1063/1.4971371/990189.
[43] W.G. Nöhring, W.A. Curtin, Correlation of microdistortions with misfit volumes in High Entropy Alloys, Scr. Mater. 168 (2019) 119–123, https://doi.org/10.1016/j.scriptamat.2019.04.012.
[44] B. Chen, S. Li, J. Ding, X. Ding, J. Sun, E. Ma, Correlating dislocation mobility with local lattice distortion in refractory multi-principal element alloys, Scr. Mater. 222 (2023) 115048, https://doi.org/10.1016/j.scriptamat.2022.115048.
[45] P. Singh, B. Vela, G. Ouyang, N. Argibay, J. Cui, R. Arroyave, D.D. Johnson, A ductility metric for refractory-based multi-principal-element alloys, Acta Mater. 257 (2023) 119104, https://doi.org/10.1016/j.actamat.2023.119104.
[46] L. Zhang, Y. Xiang, J. Han, D.J. Srolovitz, The effect of randomness on the strength of high-entropy alloys, Acta Mater. 166 (2019) 424–434, https://doi.org/10.1016/j.actamat.2018.12.032.
[47] T. Jiang, Y. Xiang, L. Zhang, Stochastic Peierls–Nabarro Model for Dislocations in High Entropy Alloys, SIAM. J. Appl. Math. 80 (2020) 2496–2517, https://doi.org/10.1137/20M1332888.
[48] W. Li, S. Lyu, Y. Chen, A.H.W. Ngan, Fluctuations in local shear-fault energy produce unique and dominating strengthening in metastable complex concentrated alloys, Proceedings of the National Academy of Sciences 120 (2023) e2209188120, https://doi.org/10.1073/pnas.2209188120.
[49] S. Lyu, W. Li, Y. Xia, Y. Chen, A.H.W. Ngan, Effects of chemical randomness on strength contributors and dislocation behaviors in a bcc multiprincipal element alloy, Phys. Rev. Mater. 7 (2023) 073602, https://doi.org/10.1103/PhysRevMaterials.7.073602.
[50] Z. Rao, P.-Y. Tung, R. Xie, Y. Wei, H. Zhang, A. Ferrari, T.P.C. Klaver, F. Körmann, P.T. Sukumar, A. Kwiatkowski da Silva, Y. Chen, Z. Li, D. Ponge, J. Neugebauer, O. Gutfleisch, S. Bauer, D. Raabe, Machine learning–enabled high-entropy alloy discovery, Science (1979) 378 (2022) 78–85, https://doi.org/10.1126/science.abo4940, 1979.
[51] Z. Pei, J. Yin, P.K. Liaw, D. Raabe, Toward the design of ultrahigh-entropy alloys via mining six million texts, Nat. Commun. 14 (1) (2023) 1–8, https://doi.org/10.1038/s41467-022-35766-5, 202314.
[52] X. Liu, J. Zhang, Z. Pei, Machine learning for high-entropy alloys: progress, challenges and opportunities, Prog. Mater. Sci. 131 (2023) 101018, https://doi.org/10.1016/J.PMATSCI.2022.101018.
[53] K. Kaufmann, K.S. Vecchio, Searching for high entropy alloys: a machine learning approach, Acta Mater. 198 (2020) 178–222, https://doi.org/10.1016/j.actamat.2020.07.065.
[54] Z. Zhou, Y. Zhou, Q. He, Z. Ding, F. Li, Y. Yang, Machine learning guided appraisal and exploration of phase design for high entropy alloys, NPJ. Comput. Mater. 5 (2019) 128, https://doi.org/10.1038/s41524-019-0265-1.

[55] Y.-J. Chang, C.-Y. Jui, W.-J. Lee, A.-C. Yeh, Prediction of the Composition and Hardness of High-Entropy Alloys by Machine Learning, JOM 71 (2019) 3433–3442, https://doi.org/10.1007/s11837-019-03704-4.
[56] C. Wen, C. Wang, Y. Zhang, S. Antonov, D. Xue, T. Lookman, Y. Su, Modeling solid solution strengthening in high entropy alloys using machine learning, Acta Mater. 212 (2021) 116917, https://doi.org/10.1016/j.actamat.2021.116917.
[57] B. Vela, C. Acemi, P. Singh, T. Kirk, W. Trehern, E. Norris, D.D. Johnson, I. Karaman, R. Arróyave, High-throughput exploration of the WMoVTaNbAl refractory multi-principal-element alloys under multiple-property constraints, Acta Mater. 248 (2023) 118784, https://doi.org/10.1016/j.actamat.2023.118784.
[58] G. Vazquez, P. Singh, D. Sauceda, R. Couperthwaite, N. Britt, K. Youssef, D. D. Johnson, R. Arróyave, Efficient machine-learning model for fast assessment of elastic properties of high-entropy alloys, Acta Mater. 232 (2022) 117924, https://doi.org/10.1016/j.actamat.2022.117924.
[59] T.Z. Khan, T. Kirk, G. Vazquez, P. Singh, A.V. Smirnov, D.D. Johnson, K. Youssef, R. Arróyave, Towards stacking fault energy engineering in FCC high entropy alloys, Acta Mater. 224 (2022) 117472, https://doi.org/10.1016/j.actamat.2021.117472.
[60] S. Zhao, R. Yuan, W. Liao, Y. Zhao, J. Wang, J. Li, T. Lookman, Descriptors for phase prediction of high entropy alloys using interpretable machine learning, J. Mater. Chem. a Mater. 12 (2024) 2807–2819, https://doi.org/10.1039/D3TA06402F.
[61] Y.N. Osetsky, D.J. Bacon, An atomic-level model for studying the dynamics of edge dislocations in metals, Model. Simul. Mat. Sci. Eng. 11 (2003) 427–446, https://doi.org/10.1088/0965-0393/11/4/302.
[62] P. Hirel, Atomsk: a tool for manipulating and converting atomic data files, Comput. Phys. Commun. 197 (2015) 212–219, https://doi.org/10.1016/j.cpc.2015.07.012.
[63] E. Bitzek, P. Koskinen, F. Gähler, M. Moseler, P. Gumbsch, Structural relaxation made simple, Phys. Rev. Lett. 97 (2006) 170201, https://doi.org/10.1103/PhysRevLett.97.170201.
[64] F. Shuang, P. Xiao, R. Shi, F. Ke, Y. Bai, Influence of integration formulations on the performance of the fast inertial relaxation engine (FIRE) method, Comput. Mater. Sci. 156 (2019) 135–141, https://doi.org/10.1016/j.commatsci.2018.09.049.
[65] J. Guénolé, W.G. Nöhring, A. Vaid, F. Houllé, Z. Xie, A. Prakash, E. Bitzek, Assessment and optimization of the fast inertial relaxation engine (fire) for energy minimization in atomistic simulations and its implementation in lammps, Comput. Mater. Sci. 175 (2020) 109584, https://doi.org/10.1016/j.commatsci.2020.109584.
[66] W.-R. Jian, Z. Xie, S. Xu, Y. Su, X. Yao, I.J. Beyerlein, Effects of lattice distortion and chemical short-range order on the mechanisms of deformation in medium entropy alloy CoCrNi, Acta Mater. 199 (2020) 352–369, https://doi.org/10.1016/j.actamat.2020.08.044.
[67] S. Yin, Y. Zuo, A. Abu-Odeh, H. Zheng, X.-G. Li, J. Ding, S.P. Ong, M. Asta, R. O. Ritchie, Atomistic simulations of dislocation mobility in refractory high-entropy alloys and the effect of chemical short-range order, Nat. Commun. 12 (2021) 4873, https://doi.org/10.1038/s41467-021-25134-0.
[68] W.-R. Jian, S. Xu, I.J. Beyerlein, On the significance of model design in atomistic calculations of the Peierls stress in Nb, Comput. Mater. Sci. 188 (2021) 110150, https://doi.org/10.1016/j.commatsci.2020.110150.
[69] A.P. Thompson, H.M. Aktulga, R. Berger, D.S. Bolintineanu, W.M. Brown, P. S. Crozier, P.J. in 't Veld, A. Kohlmeyer, S.G. Moore, T.D. Nguyen, R. Shan, M. J. Stevens, J. Tranchida, C. Trott, S.J. Plimpton, LAMMPS - a flexible simulation tool for particle-based materials modeling at the atomic, meso, and continuum scales, Comput. Phys. Commun. 271 (2022) 108171, https://doi.org/10.1016/j.cpc.2021.108171.
[70] A. Stukowski, Visualization and analysis of atomistic simulation data with OVITO–the Open Visualization Tool, Model. Simul. Mat. Sci. Eng. 18 (2010) 015012, https://doi.org/10.1088/0965-0393/18/1/015012.
[71] A. Stukowski, V.V. Bulatov, A. Arsenlis, Automated identification and indexing of dislocations in crystal interfaces, Model. Simul. Mat. Sci. Eng. 20 (2012) 085007, https://doi.org/10.1088/0965-0393/20/8/085007.
[72] C.A. Becker, F. Tavazza, Z.T. Trautt, R.A. Buarque de Macedo, Considerations for choosing and using force fields and interatomic potentials in materials science and engineering, Curr. Opin. Solid. State Mater. Sci. 17 (2013) 277–283, https://doi.org/10.1016/j.cossms.2013.10.001.
[73] X.W. Zhou, R.A. Johnson, H.N.G. Wadley, Misfit-energy-increasing dislocations in vapor-deposited CoFe/NiFe multilayers, Phys. Rev. B 69 (2004) 144113, https://doi.org/10.1103/PhysRevB.69.144113.
[74] X.W. Zhou, H.N.G. Wadley, R.A. Johnson, D.J. Larson, N. Tabat, A. Cerezo, A. K. Petford-Long, G.D.W. Smith, P.H. Clifton, R.L. Martens, T.F. Kelly, Atomic scale structure of sputtered metal multilayers, Acta Mater. 49 (2001) 4005–4015, https://doi.org/10.1016/S1359-6454(01)00287-7.
[75] S. Chen, Z.H. Aitken, S. Pattamatta, Z. Wu, Z.G. Yu, D.J. Srolovitz, P.K. Liaw, Y.-W. Zhang, Simultaneously enhancing the ultimate strength and ductility of high-entropy alloys via short-range ordering, Nat. Commun. 12 (2021) 4953, https://doi.org/10.1038/s41467-021-25264-5.
[76] B. Chen, S. Li, H. Zong, X. Ding, J. Sun, E. Ma, Unusual activated processes controlling dislocation motion in body-centered-cubic high-entropy alloys, Proceedings of the National Academy of Sciences 117 (2020) 16199–16206, https://doi.org/10.1073/pnas.1919136117.
[77] S. Xu, A. Al Mamun, S. Mu, Y. Su, Uniaxial deformation of nanowires in 16 refractory multi-principal element alloys, J. Alloys. Compd. 959 (2023) 170556, https://doi.org/10.1016/j.jallcom.2023.170556.
[78] S. Xu, Y. Su, W.-R. Jian, I.J. Beyerlein, Local slip resistances in equal-molar MoNbTi multi-principal element alloy, Acta Mater. 202 (2021) 68–79, https://doi.org/10.1016/j.actamat.2020.10.042.
[79] S.I. Rao, B. Akdim, E. Antillon, C. Woodward, T.A. Parthasarathy, O.N. Senkov, Modeling solution hardening in BCC refractory complex concentrated alloys: nbTiZr, Nb1.5TiZr0.5 and Nb0.5TiZr1.5, Acta Mater. 168 (2019) 222–236, https://doi.org/10.1016/j.actamat.2019.02.013.
[80] D. Farkas, A. Caro, Model interatomic potentials and lattice strain in a high-entropy alloy, J Mater Res 33 (2018) 3218–3225, https://doi.org/10.1557/jmr.2018.245.
[81] D. Farkas, A. Caro, Model interatomic potentials for Fe–Ni–Cr–Co–Al high-entropy alloys, J Mater Res 35 (2020) 3031–3040, https://doi.org/10.1557/jmr.2020.294.
[82] G. Bonny, D. Terentyev, R.C. Pasianot, S. Poncé, A. Bakaev, Interatomic potential to study plasticity in stainless steels: the FeNiCr model alloy, Model. Simul. Mat. Sci. Eng. 19 (2011) 085008, https://doi.org/10.1088/0965-0393/19/8/085008.
[83] W.-M. Choi, Y.H. Jo, S.S. Sohn, S. Lee, B.-J. Lee, Understanding the physical metallurgy of the CoCrFeMnNi high-entropy alloy: an atomistic simulation study, NPJ. Comput. Mater. 4 (2018) 1, https://doi.org/10.1038/s41524-017-0060-9.
[84] L. Wu, T. Li, A machine learning interatomic potential for high entropy alloys, J. Mech. Phys. Solids. 187 (2024) 105639, https://doi.org/10.1016/j.jmps.2024.105639.
[85] X.-G. Li, C. Chen, H. Zheng, Y. Zuo, S.P. Ong, Complex strengthening mechanisms in the NbMoTaW multi-principal element alloy, NPJ. Comput. Mater. 6 (2020) 70, https://doi.org/10.1038/s41524-020-0339-0.
[86] P. Yu, J.-P. Du, S. Shinzato, F.-S. Meng, S. Ogata, Theory of history-dependent multi-layer generalized stacking fault energy— A modeling of the micro-substructure evolution kinetics in chemically ordered medium-entropy alloys, Acta Mater. 224 (2022) 117504, https://doi.org/10.1016/j.actamat.2021.117504.
[87] J.-P. Du, P. Yu, S. Shinzato, F.-S. Meng, Y. Sato, Y. Li, Y. Fan, S. Ogata, Chemical domain structure and its formation kinetics in CrCoNi medium-entropy alloy, Acta Mater. 240 (2022) 118314, https://doi.org/10.1016/j.actamat.2022.118314.
[88] Y. Zuo, C. Chen, X. Li, Z. Deng, Y. Chen, J. Behler, G. Csányi, A.V. Shapeev, A. P. Thompson, M.A. Wood, S.P. Ong, Performance and Cost Assessment of Machine Learning Interatomic Potentials, J. Phys. Chem. A 124 (2020) 731–745, https://doi.org/10.1021/acs.jpca.9b08723.
[89] G. Kresse, J. Furthmüller, Efficiency of ab-initio total energy calculations for metals and semiconductors using a plane-wave basis set, Comput. Mater. Sci. 6 (1996) 15–50, https://doi.org/10.1016/0927-0256(96)00008-0.
[90] H.S. Oh, S.J. Kim, K. Odbadrakh, W.H. Ryu, K.N. Yoon, S. Mu, F. Körmann, Y. Ikeda, C.C. Tasan, D. Raabe, T. Egami, E.S. Park, Engineering atomic-level complexity in high-entropy and complex concentrated alloys, Nat. Commun. 10 (2019) 2090, https://doi.org/10.1038/s41467-019-10012-7.
[91] J. Perdew, K. Burke, M. Ernzerhof, Generalized Gradient Approximation Made Simple, Phys. Rev. Lett. 77 (1996) 3865–3868, https://doi.org/10.1103/PhysRevLett.77.3865.
[92] P.E. Blöchl, Projector augmented-wave method, Phys. Rev. B 50 (1994) 17953–17979, https://doi.org/10.1103/PhysRevB.50.17953.
[93] Y.-J. Hu, A. Sundar, S. Ogata, L. Qi, Screening of generalized stacking fault energies, surface energies and intrinsic ductile potency of refractory multicomponent alloys, Acta Mater. 210 (2021) 116800, https://doi.org/10.1016/j.actamat.2021.116800.
[94] B. Joós, M.S. Duesbery, The Peierls Stress of Dislocations: an Analytic Formula, Phys. Rev. Lett. 78 (1997) 266–269, https://doi.org/10.1103/PhysRevLett.78.266.
[95] S. Zhao, G.M. Stocks, Y. Zhang, Stacking fault energies of face-centered cubic concentrated solid solution alloys, Acta Mater. 134 (2017) 334–345, https://doi.org/10.1016/j.actamat.2017.05.001.
[96] Y. Zeng, X. Cai, M. Koslowski, Effects of the stacking fault energy fluctuations on the strengthening of alloys, Acta Mater. 164 (2019) 1–11, https://doi.org/10.1016/j.actamat.2018.09.066.
[97] M.S. Daw, S.M. Foiles, M.I. Baskes, The embedded-atom method: a review of theory and applications, Materials Science Reports 9 (1993) 251–310, https://doi.org/10.1016/0920-2307(93)90001-U.
[98] Z. Wu, H. Bei, G.M. Pharr, E.P. George, Temperature dependence of the mechanical properties of equiatomic solid solution alloys with face-centered cubic crystal structures, Acta Mater. 81 (2014) 428–441, https://doi.org/10.1016/J.ACTAMAT.2014.08.026.
[99] L. Patriarca, A. Ojha, H. Sehitoglu, Y.I. Chumlyakov, Slip nucleation in single crystal FeNiCoCrMn high entropy alloy, Scr. Mater. 112 (2016) 54–57, https://doi.org/10.1016/j.scriptamat.2015.09.009.
[100] X. Liu, Z. Pei, M. Eisenbach, Dislocation core structures and Peierls stresses of the high-entropy alloy NiCoFeCrMn and its subsystems, Mater. Des. 180 (2019) 107955, https://doi.org/10.1016/j.matdes.2019.107955.
[101] A.S.K. Mohammed, O.K. Celebi, H. Sehitoglu, Critical stress prediction upon accurate dislocation core description, Acta Mater. 233 (2022) 117989, https://doi.org/10.1016/j.actamat.2022.117989.
[102] S. Zhang, G. Wang, First principles prediction of yield strength of body centered cubic structured high entropy alloys, Mater. Today Commun. 36 (2023) 106684, https://doi.org/10.1016/j.mtcomm.2023.106684.
[103] F.R.N. Nabarro, Dislocations in a simple cubic lattice, Proceedings of the Physical Society 59 (1947) 256–272, https://doi.org/10.1088/0959-5309/59/2/309.

[104] P. Szelestey, M. Patriarca, K. Kaski, Computational study of core structure and Peierls stress of dissociated dislocations in nickel, Model. Simul. Mat. Sci. Eng. 11 (2003) 883–895, https://doi.org/10.1088/0965-0393/11/6/006.
[105] A.J. Ardell, Precipitation hardening, Metallurgical Transactions A 16 (1985) 2131–2165, https://doi.org/10.1007/BF02670416.
[106] R. Ouyang, S. Curtarolo, E. Ahmetcik, M. Scheffler, L.M. Ghiringhelli, SISSO: a compressed-sensing method for identifying the best low-dimensional descriptor in an immensity of offered candidates, Phys. Rev. Mater. 2 (2018) 083802, https://doi.org/10.1103/PhysRevMaterials.2.083802.
[107] J. Fan, J. Lv, Sure Independence Screening for Ultra-High Dimensional Feature Space, J. R. Stat. Soc. Series. B Stat. Methodol. 70 (2006) 849–911, https://doi.org/10.1111/j.1467-9868.2008.00674.x.
[108] R. Tibshirani, Regression Shrinkage and Selection Via the Lasso, J. R. Stat. Soc. Series. B Stat. Methodol. 58 (1996) 267–288, https://doi.org/10.1111/j.2517-6161.1996.tb02080.x.
[109] V.V. Bulatov, E. Kaxiras, Semidiscrete Variational Peierls Framework for Dislocation Core Properties, Phys. Rev. Lett. 78 (1997) 4221–4224, https://doi.org/10.1103/PhysRevLett.78.4221.
[110] Y. Ikeda, B. Grabowski, F. Körmann, Ab initio phase stabilities and mechanical properties of multicomponent alloys: a comprehensive review for high entropy alloys and compositionally complex alloys, Mater. Charact. 147 (2019) 464–511, https://doi.org/10.1016/j.matchar.2018.06.019.
[111] X. Liu, W.A. Curtin, Atomistic simulations reveal strength reductions due to short-range order in alloys, Acta Mater. 263 (2024) 119471, https://doi.org/10.1016/J.ACTAMAT.2023.119471.
[112] B. Yin, W.A. Curtin, First-principles-based prediction of yield strength in the RhIrPdPtNiCu high-entropy alloy, NPJ. Comput. Mater. 5 (2019) 1–7, https://doi.org/10.1038/s41524-019-0151-x, 2019 5:1.
[113] L.R. Owen, N.G. Jones, Lattice distortions in high-entropy alloys, J Mater Res 33 (2018) 2954–2969, https://doi.org/10.1557/jmr.2018.322.
[114] J. Zhang, C. Cai, G. Kim, Y. Wang, W. Chen, Composition design of high-entropy alloys with deep sets learning, NPJ. Comput. Mater. 8 (1) (2022) 1–11, https://doi.org/10.1038/s41524-022-00779-7, 20228.
[115] M.N. Magomedov, On the deviation from the Vegard's law for the solid solutions, Solid. State Commun. 322 (2020) 114060, https://doi.org/10.1016/j.ssc.2020.114060.
[116] B. Joós, Q. Ren, M.S. Duesbery, Peierls-Nabarro model of dislocations in silicon with generalized stacking-fault restoring forces, Phys. Rev. B 50 (1994) 5890, https://doi.org/10.1103/PhysRevB.50.5890.
[117] B. Xing, W. Zou, T.J. Rupert, P. Cao, Vacancy diffusion barrier spectrum and diffusion correlation in multicomponent alloys, Acta Mater. 266 (2024) 119653, https://doi.org/10.1016/j.actamat.2024.119653.
[118] Z. Xie, Y. Wang, C. Lu, L. Dai, Sluggish hydrogen diffusion and hydrogen decreasing stacking fault energy in a high-entropy alloy, Mater. Today Commun. 26 (2021) 101902, https://doi.org/10.1016/j.mtcomm.2020.101902.
[119] K.-Y. Tsai, M.-H. Tsai, J.-W. Yeh, Sluggish diffusion in Co–Cr–Fe–Mn–Ni high-entropy alloys, Acta Mater. 61 (2013) 4887–4897, https://doi.org/10.1016/j.actamat.2013.04.058.
[120] X.-Y. Zhou, J.-H. Zhu, Y. Wu, X.-S. Yang, T. Lookman, H.-H. Wu, Machine learning assisted design of FeCoNiCrMn high-entropy alloys with ultra-low hydrogen diffusion coefficients, Acta Mater. 224 (2022) 117535, https://doi.org/10.1016/j.actamat.2021.117535.
[121] S.L. Thomas, S. Patala, Vacancy diffusion in multi-principal element alloys: the role of chemical disorder in the ordered lattice, Acta Mater. 196 (2020) 144–153, https://doi.org/10.1016/j.actamat.2020.06.022.
[122] Y.-Z. Wang, Y.-J. Wang, Disentangling diffusion heterogeneity in high-entropy alloys, Acta Mater. 224 (2022) 117527, https://doi.org/10.1016/j.actamat.2021.117527.
[123] P.A. Santos-Florez, S.-C. Dai, Y. Yao, H. Yanxon, L. Li, Y.-J. Wang, Q. Zhu, X.-X. Yu, Short-range order and its impacts on the BCC MoNbTaW multi-principal element alloy by the machine-learning potential, Acta Mater. 255 (2023) 119041, https://doi.org/10.1016/j.actamat.2023.119041.
[124] H. Zheng, L.T.W. Fey, X.G. Li, Y.J. Hu, L. Qi, C. Chen, S. Xu, I.J. Beyerlein, S. P. Ong, Multi-scale investigation of short-range order and dislocation glide in MoNbTi and TaNbTi multi-principal element alloys, NPJ. Comput. Mater. 9 (1) (2023) 1–13, https://doi.org/10.1038/s41524-023-01046-z, 20239.
[125] Y. Mishin, Machine-learning interatomic potentials for materials science, Acta Mater. 214 (2021) 116980, https://doi.org/10.1016/j.actamat.2021.116980.
[126] G.P.P. Pun, R. Batra, R. Ramprasad, Y. Mishin, Physically informed artificial neural networks for atomistic modeling of materials, Nat. Commun. 10 (1) (2019) 1–10, https://doi.org/10.1038/s41467-019-10343-5, 201910.
[127] G.P.P. Pun, V. Yamakov, J. Hickman, E.H. Glaessgen, Y. Mishin, Development of a general-purpose machine-learning interatomic potential for aluminum by the physically informed neural network method, Phys. Rev. Mater. 4 (2020) 113807, https://doi.org/10.1103/PhysRevMaterials.4.113807.